e-Prime - Advances in Electrical Engineering, Electronics and Energy 11 (2025) 100870

Contents lists available at ScienceDirect

e-Prime - Advances in Electrical Engineering, Electronics and Energy

journal homepage: www.elsevier.com/locate/prime

Generalized real-time state of health estimation for lithium-ion batteries using simulation-augmented multi-objective dual-stream fusion of multi-Bi-LSTM-attention

Jarin Tasnim, Md. Azizur Rahman, Md. Shoaib Akhter Rafi, Muhammad Anisuzzaman Talukder, Md. Kamrul Hasan *

Department of Electrical and Electronic Engineering, Bangladesh University of Engineering and Technology (BUET), Dhaka, 1205, Bangladesh

ARTICLE INFO

Keywords:
Lithium-ion batteries
State of health
Energy discrepancy aware preprocessing
Overlapped data splitting
Simulation model
Attention guided multi-Bi-LSTM
Feature fusion network

ABSTRACT

To maintain the safe and reliable operation of lithium-ion batteries and manage their timely replacement, accurate state of health (SOH) estimation is critically important. This paper presents a novel deep-learning framework based on multi-loss optimized dual stream fusion of attention integrated multi-Bi-LSTM networks (multi-ABi-LSTM), for generalized real-time SOH estimation of lithium-ion batteries. Battery sensor data is first preprocessed utilizing novel energy discrepancy aware variable cycle length synchronization and grid encoding schemes to achieve generalizability considering battery sets with different discharge profiles and then passed through two parallel networks: overlapped data splitting (ODS)-based attention integrated multi-Bi-LSTM network (ODS-multi-ABi-LSTM) and past cycles' SOHs (PCSs)-based attention integrated multi-Bi-LSTM (PCS-multi-ABi-LSTM) network. The complementary features extracted from these two networks are effectively combined by a proposed fusion network to achieve high SOH estimation accuracy. Furthermore, a lithium-ion battery simulation model is employed for data augmentation during training, enhancing the generalizability of the proposed data-driven model. The suggested technique outperforms previous methods by a remarkable margin achieving 0.716% MAPE, 0.005 MAE, 0.653% RMSE, and 0.992 R^2 on a combined dataset consisting of four different battery sets with varying specifications and discharge profiles, indicating its generalization capability. Appliances using lithium-ion batteries can adopt the proposed SOH prediction framework to predict battery health conditions in real-time, ensuring operational safety and reliability.

1. Introduction

Lithium-ion batteries have widely been utilized as the primary energy storage systems for electric vehicles (EVs), smart grids, and portable electronic devices owing to their long cycle life, high energy density, low self-discharge rate, and environmental friendliness [1]. However, with repeated charge and discharge cycles, the performance of the lithium-ion batteries deteriorates due to the degradation of the electrochemical constituents, resulting in capacity fading and power decrease [2]. For lithium-ion batteries' safe and reliable operation, a battery management system (BMS) plays a vital role in continuously monitoring battery internal states [3]. The state of health (SOH) metric serves as a crucial parameter to evaluate the battery health status in the BMS, which is typically characterized as the current maximum available capacity to the nominal capacity [4]. When the battery SOH drops to 75% or 80%, it is considered the end of life (EOL) for the battery [2]. Accurate real-time estimation of battery SOH is crucial for the timely replacement of the batteries before reaching the EOL and to ensure operational safety [5].

Current methods for SOH estimation can be divided into three broad categories: direct measurement methods, model-based methods, and data-driven methods [6]. In direct estimation methods, SOH for a particular battery cycle is determined by either the decrease in maximum available capacity or the increase in internal resistance [6]. Maximum available capacity is generally obtained by the ampere-hour integration, which integrates the battery current over full charging or discharging time. However, this process requires complete charging and discharging of the battery, which is not feasible in real-life scenarios due to diverse customer habits and random operating conditions [7]. To determine the battery's internal resistance, specific laboratory equipment is strictly required [8]. Both of these direct measurement methods are only feasible for offline SOH estimation under test lab environments and not applicable for online real-time SOH estimation [6].

* Corresponding author.
E-mail address: khasan@eee.buet.ac.bd (M.K. Hasan).

https://doi.org/10.1016/j.prime.2024.100870
Received 28 July 2024; Received in revised form 31 October 2024; Accepted 1 December 2024
Available online 9 December 2024
2772-6711/© 2024 The Authors. Published by Elsevier Ltd. This is an open access article under the CC BY license (http://creativecommons.org/licenses/by/4.0/).

The model-based approaches for battery degradation estimation include two types of battery models, the electrochemical model and the equivalent circuit model. The model parameters are identified considering the aging characteristics and employed to realize battery health status [6]. The electrochemical models can accurately estimate SOH by describing the internal chemical reaction processes inside the lithium-ion battery cells [6]. Li et al. [9] proposed a reduced-order single particle model for predicting capacity fading considering the solid electrolyte interface (SEI) layer formation and its cracking due to the volume expansion of the particles in the active materials. Atalay et al. [10] utilized a pseudo-two-dimensional (P2D) electrochemical model incorporating multi-layered SEI, lithium-ion plating, and reduction of anode porosity to analyze the complex aging mechanism and capacity fading. Although these electrochemical models provide accurate SOH estimation, the determination of the model parameters requires solving complex partial differential equations, which is both time-consuming and computationally expensive for the BMS, which limits its practical applications for onboard SOH estimation.

Compared to complex electrochemical models, the equivalent circuit model (ECM) has much better online capability due to its simplified circuit architecture with classical electrical components and fewer parameters, thus simulating dynamic electrical behaviors. After the model parameters are identified, ECMs are combined with different filtering algorithms to estimate battery health status [11,12]. Ma et al. [13] proposed a fractional second-order RC model, the parameters of which are determined by an adaptive genetic algorithm, and then the unscented Kalman filter (UKF) is employed to predict SOH. To capture the Lithium-ion battery degradation, Amir et al. [14] employed a 2-RC model considering the effect of both time and temperature on capacity degradation. Although these ECM models can provide high-end performance with simplified structures, specific experimental data capturing the aging mechanism over the entire lifetime of the battery is required for model calibration [15]. Furthermore, the model parameters are susceptible to noise, operating conditions, and environmental changes. These factors limit ECM's generalization capability for diverse sets of batteries and affect the accuracy of the estimated SOH [11].

In recent years, data-driven approaches for SOH estimation have gained significant attention from researchers for their excellent self-learning capability, high adaptability, and real-time applicability without requiring any prior domain knowledge regarding battery aging or physical models [11,15]. The data-driven approaches derive manual or automated features from battery operational data and map those features for SOH prediction utilizing machine-learning or deep-learning algorithms [6,11,16]. The SOH estimation accuracy of these data-driven approaches depends on both the selection of appropriate input features and the selection of machine learning or deep learning methods. These features can be categorized into four types: voltage-related features, current-related features, temperature-related features, and incremental capacity (IC)-related features. They can be extracted for the charging or discharging cycles.

Since for lithium-ion batteries, the constant current-constant voltage (CCCV) charging principle is typically followed, the charging cycle features are generally extracted from the constant current (CC) and constant voltage (CV) phases. The features in the CC phase include CC charging time [17–20], the slope of the voltage curve at the end of CC charging [18] and charging time for a predefined voltage range [21]. CV charging time [16,18], CV capacity [16,22], average current in CV phase [16] and time interval for equal charging current difference in the CV phase [16] are some of the CV phase-based features used for battery health indication. The IC curves, derived from partial charging or discharging voltage and current data, have also frequently been used in recent research for SOH estimation. IC curve-related features include the peak and valley of the IC curve [23], area under the IC curve [24], difference between IC curve values at predefined voltage range [25], dynamic voltage warping (DVW) distance with the first cycle IC curve [26] etc. For mapping these manually designed features to battery state of health estimation, typical machine learning algorithms, including support vector machine (SVR) [17], gaussian process regression (GPR) [19], random forest (RF) [27] etc., are utilized. Lin et al. [17] utilized constant current charging time (CCCT) as input features and combined it with RF regression method to predict battery SOH. Liu et al. [16] extracted five features from the CV charging phase, such as CV charging time, charging capacity, and average current in the CV phase, and utilized both SVR and long short-term memory (LSTM) as primary and secondary learners, respectively, to estimate SOH from the five features. Li et al. [26] proposed the DVW distance between the IC curves of the current and initial discharging cycle as a health indicator (HI), enhanced the linear relationship between HI and battery health status using box-cox transformation, and finally used linear regression to predict the SOH. Although these manually extracted features from voltage, current, or IC curves of the charging or discharging phase provide highly accurate SOH estimation, they are subjected to several issues. Features based on the CC charging phase require a fixed charging starting point to be estimated accurately. However, in real-life scenarios, users tend to charge the battery before reaching full discharge resulting in random starting capacity [11]. Hence, the extracted CC features will not be accurate. CV charging features can avoid these random starting states but require full charging to estimate the features accurately, which is often not feasible in practical applications [11]. On the other hand, standard IC curves derived from charging/discharging voltage and current data suffer from low resolution during sharp voltage changes and are vulnerable to noise and interference [26]. Therefore, an additional smoothing/filtering process is required before feature extraction increasing the computational burden in real-time applications [11]. Furthermore, these methods based on manually extracted features lack generalizability for diverse sets of lithium-ion batteries in different operating conditions and suffer from feature redundancy, requiring optimization and preprocessing steps [11].

To overcome the limitations of manual feature extraction, in recent years many researchers have adopted deep learning algorithms to extract features automatically from the current, voltage, temperature or IC curve data of the battery charging or discharging cycles. Neural network models such as, LSTM [28], gated recurrent unit (GRU), Bi-LSTM [29,30], Bi-LSTM-Attention [31] and convolution neural networks (CNN) [32] have widely been used for SOH estimation in recent years. Fan et al. [6] utilized a hybrid neural network combining GRU and CNN to extract features automatically from battery full charging voltage, current and temperature curves and predict SOH. Choi et al. [33] proposed a battery capacity estimation method using FNN, CNN, and LSTM networks with full charging voltage, current and temperature data as input. However, these methods do not consider battery real-life use cases where full charging or discharging is not feasible. In this regard, recent research has adopted partial instead of full charging/discharging data to estimate battery health. Shen et al. [34] obtained voltage, current and charging capacity data from the partial charging curves and estimated battery SOH by training a deep convolutional neural network model (DCNN) with ensemble learning and transfer learning. Qian et al. [32] presented a 1D CNN model to extract features from partial charging voltage, differential voltage and current curves to provide capacity degradation information. Utilizing a simple CNN architecture, Chen et al. [11] obtained health features from partial CV charging phase current and differential current curves and estimated battery SOH. These research have preferred charging profile data for battery health prediction since the charging process typically follows a preset protocol enabling deep learning models to extract features and map to SOH easily. However, to obtain the health status of battery-powered devices during real-time operation, challenging discharge cycling sensor data carrying high randomness depending on the owner's routine needs to be utilized. Bockrath et al. [15] proposed a data-driven SOH estimation method based on a temporal convolution neural network with voltage, current and temperature data from different segments of partial discharge profiles. Lu et al. [35] used a CNN model to extract features from partial discharging profiles such as discharging capacity vs. voltage curve, IC curve and capacity changing curve to predict battery health status.

Several studies utilized LSTM-based networks for their excellent capability to capture long term temporal features. Wang et al. [36] proposed an explainability-driven model based on LSTM to guide the model using feed-back explanation for the estimation of SOH. Van et al. [28] implemented an LSTM based network for estimating SOH and internal resistance based on current, voltage and temperature. Typical LSTM networks capture features from only one direction. Therefore, Bi-LSTM networks provide a more robust performance enabling the capability to capture features from both forward and backward direction [29,30]. Moreover, by incorporating temporal attention mechanism Bi-LSTM can focus on specific positions in the sequence that are more significant than others, resulting an enhanced performance in SOH estimation [31]. Multiple studies utilized CNN and LSTM combined network to extract both short term and long term temporal dependencies [37,38]. Khan et al. [39] utilized a CNN-Bi-LSTM hybrid network to estimate the lithium-ion battery's SOH. They implemented Group Learning Algorithm (GLA) to find out the most efficient hyper-parameters of Bi-LSTM network.

While these methods use partial discharge data, they are limited by using a particular voltage or state of charge (SOC) range of the discharge cycle. This hinders the real-time continuous SOH estimation during an ongoing discharge cycle. In this respect, Qin et al. [40] proposed a similarity-analysis-based future data reconstruction method to provide the battery's SOH on the fly with partial discharge data. Their method utilized a temporal-attention-based LSTM model for feature extraction and mapping them to battery SOH.

Apart from the discussed limitations, the preprocessing scheme of the state-of-the-art methods lacks generalization to handle data from diverse sets of batteries with different discharge profiles and provide accurate SOH estimation. These methods were evaluated utilizing a particular dataset at a time containing battery cells with similar discharging profiles. Furthermore, recent research has focused more on the effect of input data (such as voltage, current, temperature, and IC curve) selection on the SOH estimation. Effects of the architectural variance, complicacy and loss functions of different deep learning algorithms on better SOH estimation accuracy are seldom explored. Additionally, these methods have not addressed the limited number of experimental datasets for training different data-driven models.

In this paper, a generalized multi-objective dual stream fusion of attention-guided multi-Bi-LSTM (multi-ABi-LSTM) network with a novel pre-processing and data augmentation scheme is presented for real-time state of health prediction of lithium-ion batteries with high accuracy. The main contributions of this work are summarized in the following:

(i) A novel pre-processing scheme with energy discrepancy aware variable cycle length (length of sampled battery data such as V, I, T) synchronization and grid encoding is proposed. The pre-processing scheme is inspired by the work of Qin et al. [40] where battery-specific variable cycle length with the increasing number of cycles was synchronized and grid encoding was proposed to magnify minor discrepancies over cycles. However, our method of cycle length synchronization and grid encoding not only synchronizes the varied cycle lengths over increasing cycles for a particular battery but also focuses on achieving generalizability for a diverse set of batteries with diverse discharge profiles, i.e., different discharging currents, operating temperatures, and rated capacities, and considers the effect of discharge current and temperature on battery SOH through grid encoding.

(ii) A temporal attention-guided Bi-LSTM network (ABi-LSTM) is utilized as the base model for feature extraction, which considers the importance of battery data features in different sampling instances of the discharging cycle for battery health prediction.

(iii) A novel fusion model, with two parallel multi-ABi-LSTM networks trained with global and local loss functions, is proposed to map the preprocessed discharge data to battery SOH. The first parallel network is the overlapped data splitting (ODS)-based multi-ABi-LSTM (ODS-multi-ABi-LSTM) network, which extracts features from overlapped discharge data segments separately with multiple ABi-LSTM networks instead of utilizing full discharge data at a time. This facilitates each ABi-LSTM network in better learning the dependencies within a particular discharge segment. Another network is the past cycles' SOHs (PCS)-based multi-ABi-LSTM (PCS-multi-ABi-LSTM) network where local losses are utilized to predict the SOHs of previous cycles and estimate the current cycle SOH in a time-series forecasting approach. This network is guided by true SOH values of both the current and previous cycles, thus achieving better SOH prediction accuracy.

(iv) Data augmentation is employed during training by generating lithium-ion battery simulation model-based cycling data. This increases the training dataset's diversity, improving the proposed data-driven model's generalization ability.

(v) The proposed framework is evaluated using four publicly available datasets and a combined dataset, for the first time to the best of our knowledge, to investigate its generalization capability for diverse sets of battery data.

2. Materials and methods

2.1. Datasets

Experiments using four publicly available lithium-ion battery datasets are used to validate our proposed method for SOH estimation. The specifications of the batteries in each of these datasets and their charging and discharging criteria are detailed in the following discussion. Table 1 presents a summary of all the datasets.

2.1.1. NASA dataset

This dataset, hosted by NASA Ames Prognostic Center of Excellence (PCoE) [41], presents data for 34 lithium-ion battery cells with a capacity of 2 Ah. The batteries were cycled until 12%, 20%, or 30% fading of initial capacity using a custom-built battery tester. The Cycling consisted of three operational profiles: charging, discharging, and impedance. For all experiments, charging followed the constant current-constant voltage (CCCV) principle, where the batteries were first charged with a constant current of 1.5 A until the battery voltage reached 4.2 V, and then the voltage remained constant at 4.2 V until the current dropped to 20 mA. However, different discharging profiles with different discharging currents and temperatures were applied to induce more realistic battery degradation. Electrochemical impedance spectroscopy (EIS) was used to measure impedance, with a frequency sweep from 0.1 Hz to 5 kHz. According to different discharging profiles, the 34 battery cells were divided into six groups. The group, consisting of batteries B0005, B0006, B0007, and B0018, which are the most widely used for SOH estimation, have been chosen for experimentation in this work. For these four batteries, charging was carried out with the CCCV criterion mentioned above, and discharging was carried out with a constant discharge current of 2 A at room temperature until the voltage fell below the discharge cut-off voltage, which is 2.7 V, 2.5 V, 2.2 V, and 2.5 V for batteries B0005, B0006, B0007, and B0018, respectively. These charging and discharging cycling experiments were continued until the batteries reached 70% of the initial rated capacity (i.e., from 2 Ahr to 1.4 Ahr), which is the defined EOL for these batteries.

Table 1
Specifications of different lithium-ion battery datasets.

Datasets	Battery ID	Rated Capacity (Ah)	Charging		Discharging		Temperature (°C)
			Constant current (A)	Maximum voltage (V)	Constant current (A)	Cut-off voltage (V)	
NASA	B0005	2	1.5	4.2	1C	2.7	24
	B0006		1.5	4.2	1C	2.5	
	B0007		1.5	4.2	1C	2.2	
	B0018		1.5	4.2	1C	2.5	
Oxford	Cell1-Cell8	0.74	0.74	4.2	1C	2.7	40
MIT	Cell 22	1.1	4.65C (44%)-5C-1C	3.6	4C	2	30
	Cell 23		4.65C (69%)-6C-1C	3.6	4C	2	
	Cell 30		4C (4%)-4.856C-1C	3.6	4C	2	
	Cell 33		5.2C (50%)-4.25C-1C	3.6	4C	2	
	Cell 35		5.2C (66%)-3.5C-1C	3.6	4C	2	
	Cell 39		5.6C (47%)-4C-1C	3.6	4C	2	
	Cell 42		5.6C (65%)-3C-1C	3.6	4C	2	
	Cell 47		6C (52%)-3.5C-1C	3.6	4C	2	
CALCE	CS2 33	1.1	0.5C	4.2	0.5C	2.7	25
	CS2 34		0.5C	4.2	0.5C	2.7	
	CS2 35		0.5C	4.2	1C	2.7	
	CS2 36		0.5C	4.2	1C	2.7	

2.1.2. Oxford dataset

The Oxford Battery Degradation Dataset, collected by the Howey Research Group, University of Oxford, in 2015 [42], contains the battery aging data of 8 Kokam lithium-ion pouch cells with a capacity of 0.74 Ah. The cells were cycled to the EOL in a thermal chamber at 40°Celsius. The degradation process involved a CCCV charging criterion with a 2C constant current and a maximum charging voltage of 4.2 V, followed by a drive cycle discharging profile derived from the Artemis Urban profile. Characterization tests were performed every 100 cycles involving a 1C constant current charge with a maximum charging voltage of 4.2 V and 1C constant current discharge with the discharge cut-off voltage set at 2.7 V. The recorded time, voltage, current, charge, and temperature from these characterization cycles are utilized in this work for SOH estimation.

2.1.3. MIT dataset

This dataset from the Massachusetts Institute of Technology and Stanford University [43] contains battery cycling data for 124 lithium-ion phosphate (LFP)/graphite cells manufactured by A123 Systems (APR18650M1 A) with a nominal capacity of 1.1 Ah. The tests were performed in a forced convection temperature chamber at 30 °C under fast charging conditions. The charging process involved a "C1(Q1)-C2" policy where the cells were first charged with constant current C1 until the SOC reached Q1 and further charged to 80% of SOC with a different constant current C2. Finally, the cells were charged under a 1C CCCV profile up to 100% of SOC with the maximum charging voltage set at 3.6 V. All cells were discharged with 4C constant current until their voltage reached the discharge cut-off at 2 V. Eight cells with different charging policies are chosen in this work for experimentation, the details of which are shown in Table 1.

2.1.4. CALCE dataset

The experimental data in this dataset was collected by the CALCE battery team at the Center for Advanced Life Cycle Engineering (CALCE), University of Maryland [44]. 15 prismatic lithium-cobalt-oxide (LCO)/graphite cells with a capacity of 1.1 Ah were cycled using the Arbin Battery Tester at room temperature. The charging procedure for all cells followed a CCCV protocol where the cells were first charged with a 0.5C constant current until the voltage reached the maximum charging voltage of 4.2 V and after that, the voltage remained constant till the current dropped to 0.05 A. The discharging was performed with a constant current rate of 0.5C or 1C until the terminal voltage reached the cut-off at 2.7 V. Two battery cells with 0.5C discharge current and two battery cells with 1C discharge current are selected in our work for SOH estimation.

2.2. Data augmentation with simulation data

The main objective of this paper is to propose a data-driven model that is well-generalized for different lithium-ion batteries with different specifications and can provide battery degradation information in real time from in-vehicle or device sensor measurements. However, training a deep learning-based model to learn the battery physics of degradation properly requires a large amount of battery data. Publicly available experimental data capturing different operating conditions is limited due to the requirement of laboratory equipment and extensive data collection time. Hence, we have utilized a lithium-ion battery simulation model to generate simulation data, which can reduce the lab time needed for data collection. With the publicly available datasets, these simulation data are added during training of the proposed data-driven model to aid in learning the varying degradation patterns of lithium-ion batteries, with cycling data from diverse operating conditions, and increase the model's generalization capability. Fig. 1(a) presents the simulation model for charging and discharging cycle data generation on MATLAB and Simulink software. The main lithium-ion battery model is represented as the 'Battery' block, which models an equivalent circuit. The circuit parameters are modified according to the discharge, temperature, and aging characteristics of a specific battery. How the equivalent circuit can approximately model a real-life lithium-ion battery considering the battery's internal temperature and aging effects are detailed in [45,46]. The circuit parameters identification is simple, requiring data from the battery datasheet, the details of which can be found in the 'Battery' block manual of the Simulink software. In this paper, the simulation data is generated for the Panasonic UR18650E lithium-ion battery with a rated capacity of 2 Ah. Some of the circuit parameters identified from the battery datasheet are presented in Table 2. The charging and discharging modes of the battery are controlled by the 'Charging/Discharging Controller' block. For simulation data generation, the battery is fully charged and discharged with constant currents of 1.5 A and 2 A, respectively, to make a complete cycle. For each cycle, battery data such as voltage, current, cell temperature, SOC, and maximum battery capacity for that cycle are collected. The cycling continued until the battery reached its EOL, i.e., 75% of its initial capacity. Sample voltage and temperature data generated from the simulation model are presented in Fig. 1(b) and (c), respectively. 10 sets of cycling data have been generated slightly varying the aging characteristics and utilized for data augmentation during training. These additional data will assist the data-driven model to more effectively learn the relationship between battery data such as voltage, current and temperature and corresponding SOH. The lithium-ion battery simulation model on Simulink software and the MATLAB code for simultaneous data collection are publicly available at this link.

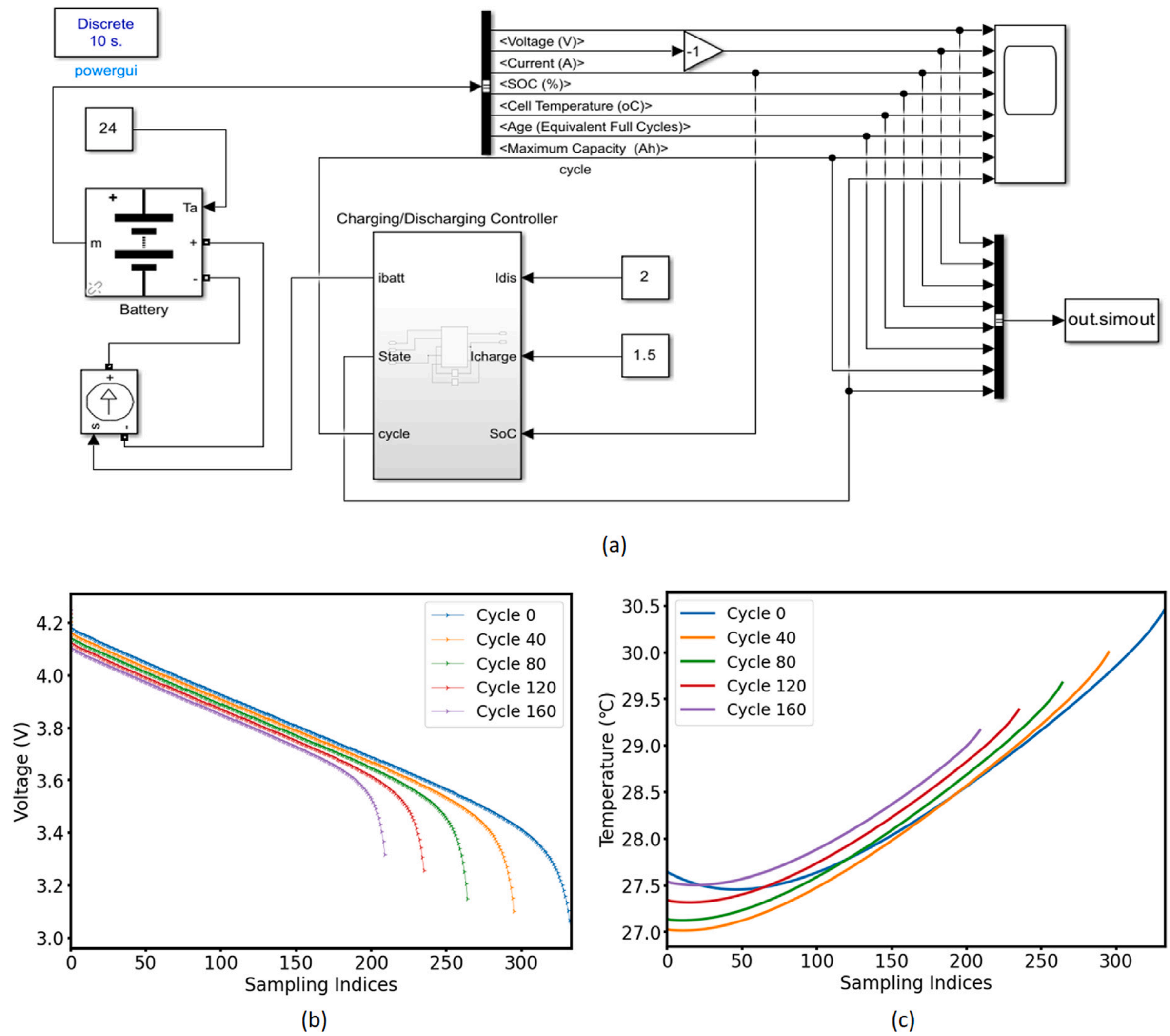

Fig. 1. Data augmentation with simulation data: (a) lithium-ion battery simulation model, sample generated data with the battery simulation model: (b) voltage; (c) temperature.

Table 2
Parameters of the simulation battery model.

Parameters	Values
Nominal voltage	3.3 V
Rated capacity	2 Ah
Maximum capacity	2.05 Ah
Cut-off voltage	2.75 V
Fully charged voltage	4.2 V
Discharge current	2 A
Charge current	1.5 A
Internal resistance	0.02 Ω
Capacity at EOL	1.5 Ah
Initial cell temperature	24 °C
Initial SOC	0%

2.3. Data analysis and preprocessing

All the datasets described previously include charging and discharging cycling data, which refers to a specific cycle's time series voltage, current, and temperature measurements during the charging and discharging process. The patterns in these voltage, current, and temperature profiles change with battery health degradation due to cycling. Some previous works on battery SOH estimation adopted cycling data during the charging process to extract features for SOH estimation since the charging follows the battery's preset CCCV protocols, whereas discharging can involve randomness involving variation in discharging currents with usage patterns and variation in ambient temperature. However, SOH estimation from charging data does not allow real-time battery health estimation during vehicle or device operation. Hence, our research investigates the relationship between discharging cycle data (i.e., voltage (V), current (I), temperature (T)) and health degradation, considering the challenges in discharge profiles with variations in discharge current and operating temperature so that battery SOH can be known in real-time directly from in-vehicle or device sensor data. The discharging cycle data are processed in two subsequent steps: (a) energy discrepancy aware variable cycle length synchronization and (b) grid encoding.

2.3.1. Energy discrepancy aware variable cycle length synchronization

As the time series discharge data were collected with different sampling rates for different datasets, the data in all the datasets are resampled with a sampling interval of 10s for generalization purposes. Fig. 2(a)–(d) and Fig. 2(e)–(h) show the variation in discharge voltage lengths and decrease in SOH with the increasing number of cycling for NASA, Oxford, MIT, and CALCE datasets, respectively.

Since the maximum available capacity decreases with cycling, the discharge time for the cells reduces, and so does the length of the sampled data. Hence, the variable length over the cycles can play an important role as a battery health indicator. However, training a data-driven model with the discharging data profile and corresponding SOH requires the data length to be the same for all cycles.

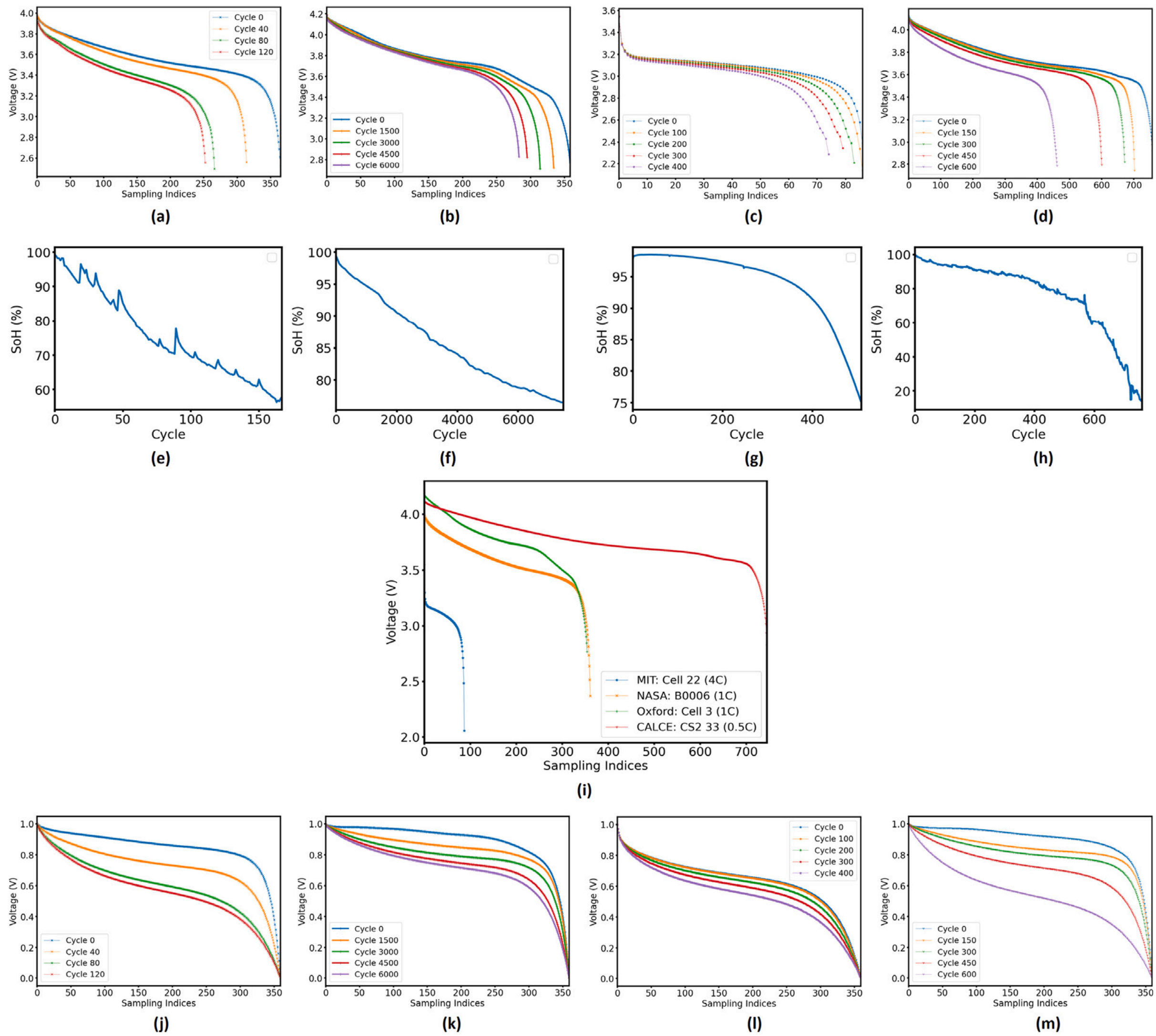

Fig. 2. Discharging voltage profiles with an increasing number of cycles: (a) NASA; (b) Oxford; (c) MIT; (d) CALCE, SOH (%) vs cycle plots: (e) NASA; (f) Oxford; (g) MIT; (h) CALCE, (i) variation in discharging voltage lengths across different cells with different discharging currents despite the same SOH (here 98%), discharging voltage profiles with increasing number of cycles after energy discrepancy aware cycle length synchronization: (j) NASA; (k) Oxford; (l) MIT; (m) CALCE.

In addition, although directly relating variable cycle length to battery SOH can provide useful information for battery health for a single battery with the same discharging current for all cycles, it can be misleading for two different batteries with different discharging currents or for a single battery with different discharging currents over the cycles. Such an example is shown in Fig. 2(i) where the discharging voltage lengths for the four cells are different despite having the SOH. As shown in the figure, the four cells are discharged with 4C, 1C, and 0.5C rates, respectively. A C-rating is defined as the battery charge or discharge current normalized against the battery-rated capacity. For a battery of 2 Ah, a 1C rate denotes a 2 A discharge current to discharge the entire battery in 1/C-rate = 1 h. Similarly, for a 2C rate, the discharge current is 4 A, and the time to full discharge is 1/C-rate = $1/2 = 0.5$ hour. In our case, the four cells from MIT, NASA, Oxford, and CALCE datasets have different discharging times owing to different discharging C-rates. This leads to variable cycle length after sampling despite having the same state of health. However, if we are to develop a generalized model for these four cells, the discharge cycle voltage data are required to be of the same length for the same battery health status.

Therefore, a generalized synchronization approach is required, which will align the discharge voltage curves over the cycles (as shown in Fig. 2(a)–(d)) while preserving the indication of different SOH and ensuring the same cycle length for the same SOH despite different discharge current rates (see Fig. 2(i)). In this regard, an energy discrepancy-aware variable cycle length synchronization approach is proposed in this work. Since the variation in cycle length also indicates the energy discrepancy across the cycles, this approach ensures energy conservation before and after synchronization. The energy before synchronization is calculated as $\sum_{k=1}^{N} \mathbf{v_c}(k)\mathbf{i_c}(k)\Delta t_c$ where $\mathbf{v_c} \in R^N$, $\mathbf{i_c} \in R^N$, Δt_c and N denotes the sampled discharging voltage, current, corresponding sampling time interval and cycle length before synchronization, for a specific cycle c. To synchronize the voltage data, a fixed discharge current rate i_s and sampling rate Δt_s are chosen for all cycles so that the modified sampled voltages $\mathbf{v_s} \in R^{N_s}$ after synchronization achieve the same length N_s. In this work, i_s is chosen as 1C for a discharging time of 1 h and t_s as 10 s, which results in a target length N_s= 1h/10s = 360. The synchronized voltage $\mathbf{v_s} \in R^{360}$ is required to be determined such that the equation of energy $\sum_{k=1}^{N} \mathbf{v_c}(k)\mathbf{i_c}(k)\Delta t_c = \sum_{k=1}^{360} \mathbf{v_s}(k) i_s \Delta t_s$ is satisfied. The algorithm to determine the synchronized voltage data $\mathbf{v_s}$ is detailed in Algorithm 1.

Fig. 2(j)–(m) presents the synchronized discharge voltage profiles with cycling, which were of variable lengths in Fig. 2(a)–(d), for the NASA, Oxford, MIT, and CALCE datasets, respectively. From Fig. 2(j)–(m), it is to be noted that the health degradation over the cycles

Algorithm 1 Iterative Solution for Variable Cycle Length Synchronization.

1: **Input:** $\mathbf{v_c}$, $\mathbf{i_c}$, Δt_c
2: **Output:** $\mathbf{v_s}$
3: Scale $\mathbf{v_c}$ dividing by the maximum possible voltage at the start of discharging which is the maximum charging voltage for a specific battery.
$\mathbf{v_{cs}} = \mathbf{v_c}/\text{Maximum charging voltage}$
4: Calculate the target electrical energy
$E_T = \sum_{k=1}^{N} \mathbf{v_{cs}}(k)\mathbf{i_c}(k)\Delta t_c$
5: Interpolate $\mathbf{v_{cs}}$ to achieve target cycle length N_s which is 360 in this work.
$\mathbf{v_{int}} = f_{interp}(\mathbf{v_{cs}})$, $\mathbf{v_{int}} \in R^{360}$
6: Define a window, $\mathbf{w} \in R^{360}$. For $k = 1, 2, \dots, 360$
$w_1(k,a) = (1-a)\exp\left(-\frac{k^{0.9}}{100a}\right) + a$
$w_2(k,a) = -w_1(360-k, 1-a) + 1$
$w_3(k) = \left(1 - \left(\frac{|k-180|}{180}\right)^4\right)\exp\left(-\left(\frac{|k-180|}{180}\right)^3\right)$
7: **if** $a > 0.9$ **then**
8: $w(k,a) = w_1(k,a)(\frac{360-k}{360}) + w_2(k,a)(\frac{k}{360}) + 10w_3(k)(a-0.9)$
9: **else**
10: $w(k,a) = w_1(k,a)(\frac{360-k}{360}) + w_2(k,a)(\frac{k}{360})$
11: **end if**
12: Define $A = 1/v_{int}(0)$
13: Initialize $a = 0.001$ and $step = 1$
14: Calculate $v_s(k) = Av_{int}(k)w(k),\ k = 1, 2, \dots, 360$
15: Define $i_s = 1C$ and $t_s = 10$
16: Calculate the electrical energy after synchronization, $E_S = \sum_{k=1}^{N_s} v_s(k) i_s \Delta t_s$
17: **while** True **do**
18: $a = a + step$
19: Calculate $\mathbf{w}$ with new a
20: Calculate $\mathbf{v_s}$ and E_S^{new} with new $\mathbf{w}$, with steps 12 and 15 respectively
21: **if** $|E_S^{new} - E_T| < 0.001$ **then**
22: **return** $\mathbf{v_s}$
23: **end if**
24: **if** $E_S^{new} > E_T$ **then**
25: $a = a - step$
26: $step = step/2$
27: **else**
28: $E_S = E_S^{new}$
29: **end if**
30: **end while**

can now be characterized by the variation of voltage values over the sampling instants (within the synchronized cycle length 360) instead of variable cycle lengths.

The sampled discharge current $\mathbf{i_c}$ and temperature $\mathbf{t_c}$ are almost constant over the cycles for all four datasets. Hence, to synchronize the variable length current and temperature data of increasing cycles to the target length $N_s = 360$, a simple interpolation approach is adopted, which can be formulated as follows:

$$\mathbf{i_s} = f_{interp}(\mathbf{i_c}) \tag{1}$$

$$\mathbf{t_s} = f_{interp}(\mathbf{t_c}) \tag{2}$$

where $\mathbf{i_s} \in R^{360}$ and $\mathbf{t_s} \in R^{360}$ refers to the synchronized discharge current and temperature data, respectively.

2.3.2. Grid encoding

The synchronized voltage, current, and temperature data obtained from the previous step are further encoded to construct the final preprocessed input vector for SOH estimation. The encoding procedures for each of these synchronized data are detailed in the following.

(1) Voltage encoding: Fig. 2(j)–(m) shows the variation of the synchronized discharge voltage curves over the cycles. The discrepancy over the cycles along the voltage axis can act as a potential battery health indicator. However, the discrepancy from one cycle to the next is minor. To magnify this minor discrepancy, the voltage value at each sampling instant is encoded as a L_v dimensional vector through grid encoding.
Let the range of the synchronized voltages over the cycles be defined as $[v_{min}, v_{max}]$. If L_v denotes the total number of grids, then the scope of grid $l_v \in [1, L_v]$ is defined as $[v_{max} - (l_v - 1)\Delta, v_{max} - l_v\Delta]$, where $\Delta = \frac{v_{max} - v_{min}}{L_v}$. For the synchronized voltage data $\mathbf{v_s} \in R^{360}$ corresponding to a particular cycle, the value of the kth sample $\mathbf{v_s}(k)$ ($k = 1, 2, \dots, 360$) is encoded with the L_v grids such that the value of the grid, within which range $\mathbf{v_s}(k)$ falls, is set as 1 and the rest $(L_v - 1)$ grid values are set as 0. With the values of v_{max}, v_{min}, and L_v being set at 1, 0, and 100, respectively, the one-dimensional synchronized voltage data $\mathbf{v_s} \in R^{360}$ is now transformed to the two dimensional encoded voltage $\mathbf{V_{enc}} \in R^{100\times360}$. Fig. 3 illustrates this transformation for a specific cycle in the NASA B0005 battery cell.
For a battery cell with C number of cycles up to the EOL, the encoded discharged voltages can be represented as $\tilde{V_{enc}} = [\mathbf{V^1_{enc}}, \mathbf{V^2_{enc}}, \dots, \mathbf{V^C_{enc}}]$ where $\mathbf{V^c_{enc}} \in R^{100\times360}$ and $c = 1, 2, \dots, C$. At any sampling instant k, the discrepancy between two cycles m and n will be measured through two 100 dimensional encoded vectors, $\mathbf{V^m_{enc}}(k) \in R^{100\times1}$ and $\mathbf{V^n_{enc}}(k) \in R^{100\times1}$ instead of two scalar values. This facilitates enlarging the minor discrepancies between two cycles over all the sampling instances of the synchronized voltage data and, hence, can better model the differences in the battery SOH with increased cycling.

(2) Current encoding: As shown in Table 1, the discharge currents for the four datasets vary in C-rates, which can affect the battery health degradation. In order to model the effect of the discharge current rate on the battery state of health, the synchronized current data $\mathbf{i_s} \in R^{360}$ is encoded as a L_i dimensional vector between the maximum and minimum C-rates of 0 and 20C at each sampling instant k ($k = 1, 2, \dots, 360$).
In this regard, the range for grid encoding is set as $[i_{min}, i_{max}] = [0, 20C]$. With L_i denoting the total number of grids in this range, the scope of grid $l_i \in [1, L_i]$ is defined as $[i_{max} - (l_i - 1)\Delta, i_{max} - l_i\Delta]$, where $\Delta = \frac{i_{max} - i_{min}}{L_i}$. Similar to voltage encoding, the current value at any sampling instant k is assigned to one of the grids, and the value of that grid is set as 1. The value of the rest $L_i - 1$ grids are set as 0. With $L_i = 100$, the one-dimensional synchronized current data $\mathbf{i_s} \in R^{360}$ obtained from the previous step is transformed to a two-dimensional encoded current $\mathbf{I_{enc}} \in R^{100\times360}$ for a particular discharge cycle. If there are total C number of cycles up to the end of life, the encoded discharge current data can be represented as $\tilde{I_{enc}} = [\mathbf{I^1_{enc}}, \mathbf{I^2_{enc}}, \dots, \mathbf{I^C_{enc}}]$ where $\mathbf{I^c_{enc}} \in R^{100\times360}$ and $c = 1, 2, \dots, C$.

(3) Temperature encoding: Similar to the discharge current, the operating temperature varies across the four datasets, as shown in Table 1. The ambient temperature affects the internal heating of battery cells and thus causes an impact on the battery health degradation. To relate the cell temperature to the battery SOH, the synchronized temperature data $\mathbf{t_s} \in R^{360}$ is encoded as a L_t dimensional vector between the maximum and minimum temperature of 1°Celsius and 50°Celsius at each sampling instant k ($k = 1, 2, \dots, 360$).
The range for grid encoding is set as $[t_{min}, t_{max}] = [1°Celsius, 50°Celsius]$. With the total number of grids $L_t = 100$, the one-dimensional synchronized temperature data $\mathbf{t_s} \in R^{360}$ for a specific discharge cycle is transformed to a two-dimensional matrix $\mathbf{T_{enc}} \in R^{100\times360}$, following the similar grid encoding procedure for voltage and current encoding. The encoded temperature data for C number of cycles can be represented as a 3D

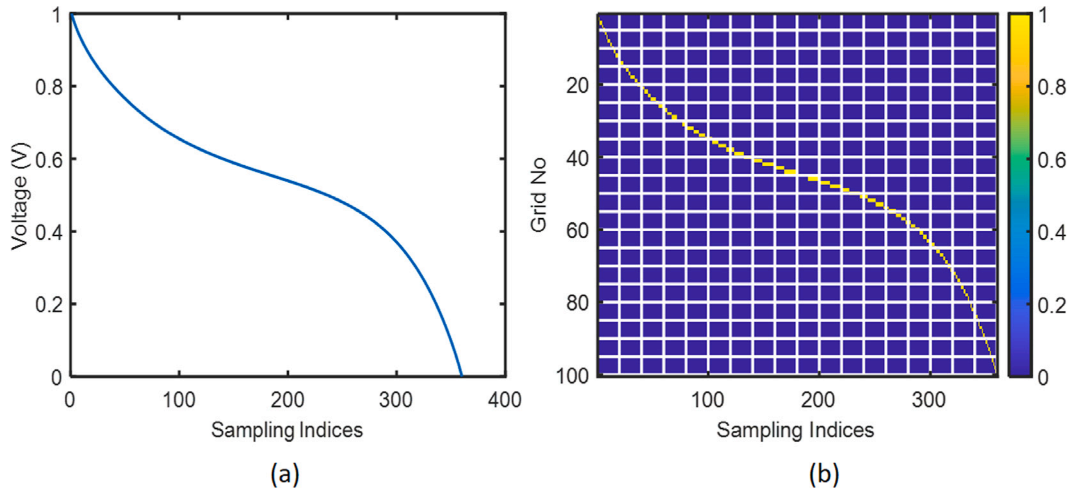

Fig. 3. Encoding of voltage data: (a) synchronized one-dimensional discharge voltage data; (b) encoded two-dimensional discharge voltage data.

data matrix, $\mathbf{T}_{enc}^{\sim} = [\mathbf{T}_{\mathbf{enc}}^{\mathbf{1}}, \mathbf{T}_{\mathbf{enc}}^{\mathbf{2}}, \dots, \mathbf{T}_{\mathbf{enc}}^{\mathbf{C}}]$, where $\mathbf{T}_{\mathbf{enc}}^{\mathbf{c}} \in R^{100\times360}$ and $c = 1, 2...C$.

The encoded voltage $\mathbf{V}_{\mathbf{enc}}^{\mathbf{c}} \in R^{100\times360}$, current $\mathbf{I}_{\mathbf{enc}}^{\mathbf{c}} \in R^{100\times360}$ and temperature data $\mathbf{T}_{\mathbf{enc}}^{\mathbf{c}} \in R^{100\times360}$ are concatenated to obtain the final 2D preprocessed matrix $\mathbf{X}_{\mathbf{enc}}^{\mathbf{c}} \in R^{300\times360}$ for a particular cycle c. This 2D matrix will serve as an input sample to our proposed model for SOH estimation. The corresponding label is the SOH for that particular cycle c, calculated as in the following:

$$SOH^c = \frac{MAC^c}{Rated\ Capacity} \tag{3}$$

where MAC^c refers to the maximum available capacity for the particular cycle c.

2.4. Proposed network architecture

This work proposes a fusion model with two parallel multi-ABi-LSTM networks, trained with multiple loss functions, to map the input feature matrices obtained after data preprocessing to their corresponding SOHs. The proposed framework for SOH estimation is illustrated in Fig. 4. For a specific cycle c, the 2D input feature matrix $\mathbf{X}_{\mathbf{enc}}^{\mathbf{c}} \in R^{300\times360}$ pass through two parallel networks, namely overlapped data splitting based multi-ABi-LSTM (ODS-multi-ABi-LSTM) network, and past cycles' SOHs based multi-ABi-LSTM (PCS-multi-ABi-LSTM) network. The two feature vectors obtained from two parallel networks enter into a fusion network, which outputs the final predicted SOH. The architectures of the parallel networks and the feature fusion network are detailed in the following subsections.

2.4.1. Overlapped data splitting based multi-ABi-LSTM networks

The appropriate modeling of multivariate time-series data is crucial for improving the prediction accuracy of SOH. Traditional time series models, e.g. ARIMA [47], only capture linear data relationships, leading to unsatisfactory predictions for nonlinear problems. Shallow machine learning models have simple structures, poor generalization, and tend to fall into local optima. Recurrent neural networks (RNN) typically performs well to capture features from time series data compared to other methods. The basic RNN is a type of artificial neural network with feedback connections that can effectively model time-series data by correlating the sequential data points [48]. However, RNN suffers from vanishing/exploding gradient problems in sequential data with long-term dependencies. The LSTM network was designed to improve RNN with additional memory cells and gating mechanisms that can capture the long-term dependencies in time-series data [49]. Although LSTM eliminates the problem of vanishing gradients in RNN and handles long-term dependencies, its accuracy is limited to processing the input sequence data in one direction, i.e., from the past to the present, thus capturing only the preceding context.

To address this issue, the Bi-LSTM processes information in both forward and backward directions, considering both past and future contexts [50]. This bidirectional approach enables the model to capture dependencies more effectively than traditional CNNs, RNNs, and LSTMs, leading to improved prediction accuracy. Additionally, its flexible architecture allows for customization with added layers like convolutional or attention layers, enhancing performance and providing a comprehensive view of sequence trends through concatenated hidden layers in both directions [39,51]. It also exhibits high robustness in time-series data modeling, effectively capturing long-term dependencies [47]. The use of dropout prevents overfitting, leading to improved generalization of the model. Consistently, Bi-LSTM outperforms LSTMs and CNNs in prediction tasks, inspiring the selection of this model for SOH estimation in our work.

As shown in Fig. 5(b), the Bi-LSTM comprises two separate LSTM cells with their own set of parameters for processing the input in forward and backward directions. In the forward processing, the information from the previous time step is considered, whereas, in the reverse processing, the information from the future time step is considered. The forward and reverse hidden states at each time step in the sequence are concatenated to get the final hidden states. Therefore, to establish a Bi-LSTM network, the processing of an LSTM cell is explained first.

As shown in Fig. 5(c), at any time step, the LSTM cell has three inputs: input for the current time step $\mathbf{x}_t \in R^{d_x\times1}$, hidden state from the previous time step $\mathbf{h}_{t-1} \in R^{d_h\times1}$ acting as a short term memory and cell state from the previous time step $\mathbf{c}_{t-1} \in R^{d_c\times1}$ acting as a long term memory. The recent past information, i.e., the short-term memory $\mathbf{h}_{t-1}$ and current time step input $\mathbf{x}_t$ are combined in a controllable way through the gating mechanism to update the long-term memory, i.e., cell state from $\mathbf{c}_{t-1}$ to $\mathbf{c}_t$. The new cell state $\mathbf{c}_t$ is used in turn to update the hidden state from $\mathbf{h}_{t-1}$ to $\mathbf{h}_t$. The hidden state $\mathbf{h}_t$ is also the output of the LSTM at time step t and it is utilized for performing a specific task.

The information flow through the LSTM cell is controlled by three gates: the forget gate, the input gate, and the output gate. The forget gate $\mathbf{f}_t$ determines which information in the cell state vector from the previous time step should be kept and which should be forgotten. It is calculated as

$$\mathbf{f}_t = \sigma\left(\mathbf{W}_{xf}\mathbf{x}_t + \mathbf{W}_{hf}\mathbf{h}_{t-1} + \mathbf{b}_f\right) \tag{4}$$

where $\mathbf{W}_{xf} \in R^{d_c\times d_x}$, $\mathbf{W}_{hf} \in R^{d_c\times d_h}$, $\mathbf{b}_f \in R^{d_c\times1}$, and $\mathbf{f}_t \in R^{d_c\times1}$. With the sigmoid activation, the value of $\mathbf{f}_t$ is between 0 and 1, and will be

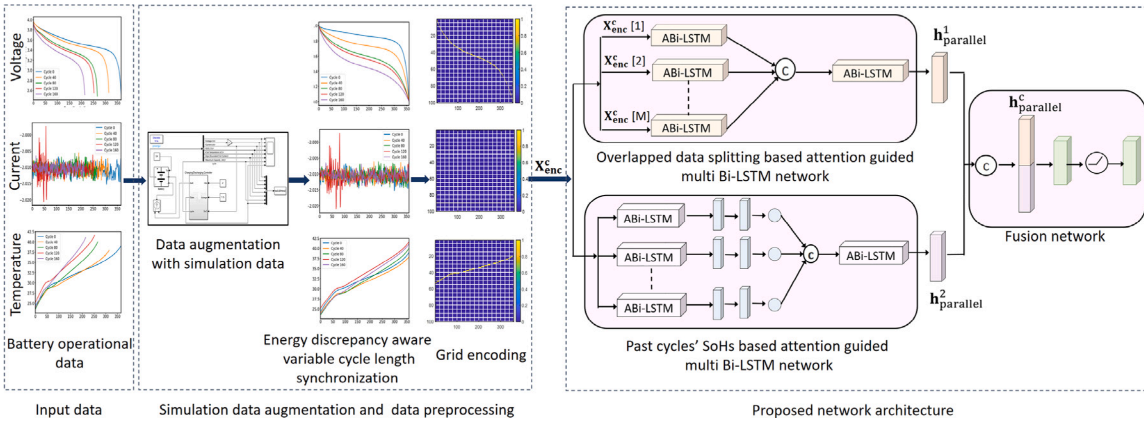

Fig. 4. Schematic for the proposed deep learning framework for SOH estimation.

elementwise multiplied with the previous cell state vector $\mathbf{c}_{t-1}$. Hence, it acts as a selector vector such that the position where $\mathbf{f}_t = 0$, the cell state information is completely forgotten, and the position where $\mathbf{f}_t = 1$, the cell state information remains completely unchanged.

After removing the irrelevant past information from the cell state, new information can be added to the cell state through the input gate. The input gate $\mathbf{i}_t$ and candidate vector $\tilde{\mathbf{c}}_t$ are calculated as follows:

$$\mathbf{i}_t = \sigma\left(\mathbf{W}_{xi}\mathbf{x}_t + \mathbf{W}_{hi}\mathbf{h}_{t-1} + \mathbf{b}_i\right) \tag{5}$$

$$\tilde{\mathbf{c}}_t = \tanh\left(\mathbf{W}_{xc}\mathbf{x}_t + \mathbf{W}_{hc}\mathbf{h}_{t-1} + \mathbf{b}_c\right) \tag{6}$$

where $\mathbf{W}_{xi} \in R^{d_c\times d_x}$, $\mathbf{W}_{hi} \in R^{d_c\times d_h}$, $\mathbf{b}_i \in R^{d_c\times 1}$, $\mathbf{i}_t \in R^{d_c\times 1}$, $\mathbf{W}_{xc} \in R^{d_c\times d_x}$, $\mathbf{W}_{hc} \in R^{d_c\times d_h}$, $\mathbf{b}_c \in R^{d_c\times 1}$, and $\tilde{\mathbf{c}}_t \in R^{d_c\times 1}$. The candidate vector $\tilde{\mathbf{c}}_t$ implies the information that is a candidate to be added to the cell state. Since $\tilde{\mathbf{c}}_t$ will be element-wise multiplied with $\mathbf{i}_t$, the input gate ranging from 0 to 1 acts as a selector vector for the candidate information. In addition, the tanh activation limits $\tilde{\mathbf{c}}_t$ between -1 and 1 so that with positive and negative values, the new information can be either added or subtracted. Finally, the updated cell state $\mathbf{c}_t$ for the current time step t is calculated by combining the past and new information passed through the forget gate and input gate as

$$\mathbf{c}_t = \mathbf{f}_t \odot \mathbf{c}_{t-1} + \mathbf{i}_t \odot \tilde{\mathbf{c}}_t \tag{7}$$

where $\odot$ denotes element-wise multiplication. The current cell state $\mathbf{c}_t$ filtered through an output gate $\mathbf{o}_t$ provides the hidden state or output $\mathbf{c}_t$ at current time step t. The process can be described as

$$\mathbf{o}_t = \sigma\left(\mathbf{W}_{xo}\mathbf{x}_t + \mathbf{W}_{ho}\mathbf{h}_{t-1} + \mathbf{b}_o\right) \tag{8}$$

$$\mathbf{h}_t = \mathbf{o}_t \odot \tanh\left(\mathbf{c}_t\right) \tag{9}$$

where $\mathbf{W}_{xo} \in R^{d_c\times d_x}$, $\mathbf{W}_{ho} \in R^{d_c\times d_h}$, $\mathbf{b}_o \in R^{d_c\times 1}$, and $\mathbf{o}_t \in R^{d_c\times 1}$. The sigmoid-activated values of $\mathbf{o}_t$ between 0 and 1 select the parts of cell state $\mathbf{c}_t$ that we want to output. The cell state vector is passed through a tanh activation before elementwise multiplication with $\mathbf{o}_t$. This ensures that the values of $\mathbf{h}_t$ are between -1 and 1 and helps to control the network's stability over time.

In the forward processing, the information from the previous time step is considered, whereas, in the reverse processing, the information from the future time step is considered. The forward and reverse hidden states at each time step in the sequence are concatenated to get the final hidden states. The procedure can be expressed as follows:

$$\mathbf{h}^{+}_t = \overrightarrow{\mathrm{LSTM}}\left(\mathbf{h}_{t-1}, \mathbf{x}_t, \mathbf{c}_{t-1}\right) \tag{10}$$

$$\mathbf{h}^{-}_t = \overleftarrow{\mathrm{LSTM}}\left(\mathbf{h}_{t+1}, \mathbf{x}_t, \mathbf{c}_{t+1}\right) \tag{11}$$

$$\mathbf{h}^{c}_t = \left[\mathbf{h}^{+}_t, \mathbf{h}^{-}_t\right] \tag{12}$$

where $\mathbf{h}^{+}_t \in R^{d_h\times 1}$, $\mathbf{h}^{-}_t \in R^{d_h\times 1}$, and $\mathbf{h}^{c}_t \in R^{2d_h\times 1}$ refer to the forward, backward and the concatenated hidden states at time step t, respectively. For a total T number of time steps ($t = 1, 2, \ldots, T$), the hidden states can be represented as

$$\tilde{\mathbf{H}}^{c} = [\mathbf{h}^{c}_1, \mathbf{h}^{c}_2, \ldots, \mathbf{h}^{c}_T] \tag{13}$$

where $\tilde{\mathbf{H}}^{c} \in R^{2d_h\times T}$.

The significance of features at various locations in the output of Bi-LSTM ($\tilde{\mathbf{H}}^{c}$) is not the same. The Attention Mechanism (AM) addresses this by assigning weights, distinguishing the importance of different positions in the sequence, similar to how the human brain focuses on specific areas. During model training, it learns and integrates these attention levels, enhancing model accuracy. This optimal weighting of features at different sequence locations improves the model's ability to predict from complex input data patterns. For our specific task of SOH estimation using Bi-LSTM, the hidden state information at each time step of the battery health data may not be equally important. To dynamically calculate the importance of each time step, a temporal attention module is proposed in this paper. In general, the inclusion of an attention layer at the output of Bi-LSTM layer (see Fig. 5(b)) increases the model's performance [52]. The attention module in our work, takes the 2D matrix $\tilde{\mathbf{H}}^{c}$ as input and provides an attention score for the hidden states at each time step. The attention score is calculated as

$$\boldsymbol{\alpha} = \mathrm{Softmax}\left(\tanh\left(\mathbf{W}_h\tilde{\mathbf{H}}^{c} + \mathbf{b}_h\right)\right) \tag{14}$$

where $\mathbf{W}_h \in R^{1\times 2d_h}$, $\mathbf{b}_h \in R^{1\times T}$, and $\boldsymbol{\alpha} \in R^{1\times T}$. The final hidden state is obtained by a weighted sum of the hidden states at each time step, where the weight corresponds to their attention score, followed by a ReLU activation layer. It can be expressed as

$$\mathbf{h}_{aB} = ReLU\left(\sum_{t=1}^{T}\alpha_t\mathbf{h}^{c}_t\right) \tag{15}$$

where $\mathbf{h}_{aB} \in R^{2d_h\times 1}$, $\alpha_t \in R^{1}$, and $\mathbf{h}^{c}_t \in R^{2d_h\times 1}$. $\mathbf{h}_{aB}$ is considered as the output from the ABi-LSTM module.

As shown in Fig. 5(a), the ODS-multi-ABi-LSTM network takes the encoded data matrix $\mathbf{X}^{\mathbf{c}}_{\mathbf{enc}} \in R^{300\times 360}$ as input. The data is then split into overlapping segments across the time dimension, i.e., along the dimension of synchronized cycle length, which is 360 in our case. Let the segment length be L, and the overlap between two segments is OL such that $O \in [0, 1]$, then the offset D is defined as $L - OL$. If there are total M no of. overlapped segments, then the equation for the mth segment ($m = 0, 1, \ldots, M-1$) can be expressed as

$$\mathbf{X}^{\mathbf{c}}_{\mathbf{enc}}[m] = \mathbf{X}^{\mathbf{c}}_{\mathbf{enc}}[Dm : Dm + L, :] \tag{16}$$

where $\mathbf{X}^{\mathbf{c}}_{\mathbf{enc}}[\mathbf{m}] \in R^{300\times L}$. In our paper, the values of L, O, and M are chosen as 288, 0.75, and 2, respectively. The offset D is calculated as, $L - OL = 288 - 0.75 \times 288 = 72$. With the value of D, the mth segment ($m = 0, 1$) data is obtained using Eq. (16).

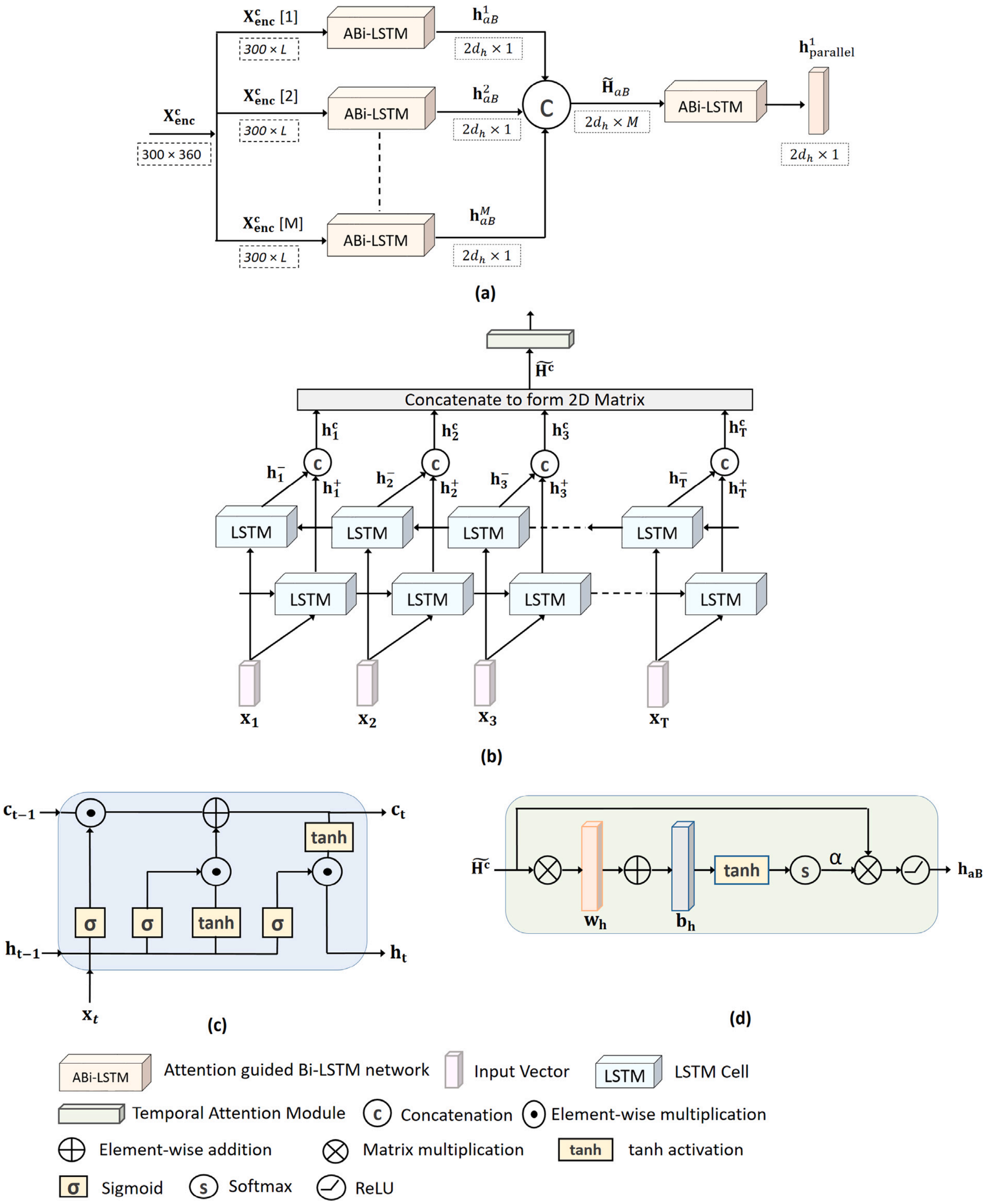

Fig. 5. (a) Architecture of the ODS-multi-ABi-LSTM network; (b) architecture of the ABi-LSTM network; (c) the structure of an LSTM cell; (d) architecture of the temporal attention module.

Each of the M data segments passes through separate ABi-LSTM modules to obtain M no of hidden state features. For the mth data segment, the input to the ABi-LSTM is $\mathbf{X}^{\mathbf{c}}_{\mathbf{enc}}[\mathbf{m}] \in R^{300\times L}$. If the input is unfolded in time steps, then in Fig. 5(b) showing the architecture of ABi-LSTM, the total number of time steps, $T = L$ and the input at each time step is $\mathbf{x}_t = \mathbf{x}^c_{enc}[m] \in R^{300\times 1}$. Following Eqs. (10) to (15), the final hidden state output $\mathbf{h}^m_{aB}$ for the mth segment obtained as

$$\mathbf{h}^m_{aB} = f^m_{ABi-LSTM}\left(\mathbf{X}^{\mathbf{c}}_{\mathbf{enc}}[\mathbf{m}]\right), m = 1, 2, \dots, M \tag{17}$$

where $\mathbf{h}^m_{aB} \in R^{2d_h\times 1}$ and $f^m_{ABi-LSTM}$ refer to the mth ABi-LSTM network.

The M hidden states obtained for M overlapped data segments are concatenated to form a 2D matrix $\tilde{\mathbf{H}}_{aB} \in R^{2d_h\times M}$. The combined matrix $\tilde{\mathbf{H}}_{aB}$ serves as an input to another ABi-LSTM network such that the total number of time steps, $T = M$ and the input at the tth time step, $\mathbf{x}_t = \mathbf{h}^t_{aB} \in R^{2d_h\times 1}$ $(t = 1, 2, \dots .M)$. Following the Eqs. (10) to (15), the final hidden state output can be obtained. The process can be formulated as

$$\mathbf{h}^{1}_{parallel} = f_{ABi-LSTM}\left(\tilde{\mathbf{H}}_{aB}\right) \tag{18}$$

where $\mathbf{h}^{1}_{parallel} \in R^{2d_h \times 1}$ refers to the output of the ABi-LSTM network $f_{ABi-LSTM}$ and also the final output feature from the first parallel network in Fig. 5(a).

Instead of a single ABi-LSTM with full data input here, we have adopted an ODS-multi-ABi-LSTM network. The main motivation behind this is that each of the parallel ABi-LSTM modules in Fig. 5(a) is required to focus only on a particular part of the sequential data, which makes it easier for the network to effectively learn the dependencies within that sequence compared to processing the whole data sequence at a time. In addition, because of the overlapping of data segments, there is a pseudo increase of data points which further improves the model's performance.

2.4.2. Past cycles' SOHs based multi-ABi-LSTM networks

The battery SOH for a particular cycle c can be predicted from the SOHs of the previous P number of cycles using a time series forecasting approach [33]. However, actual SOHs for each of the battery cycles up to the EOL are only available in the training data through experimental measurements. During real-time testing of cth battery cycle, true SOHs of P previous cycles cannot be obtained. However, since the SOHs of a small number of consecutive cycles are quite close to each other, we try to predict the SOHs of the P number of past cycles, i.e., cycle $(c-P)$ to cycle $(c-1)$ with the real-time sensor measurements data of the present cycle c utilizing a local loss based approach. The predicted SOHs are then utilized to forecast the SOH for cycle c. As shown in Fig. 6(a), the past cycles' SOHs based multi-ABi-LSTM network takes the preprocessed 2D input data matrix $\mathbf{X}^{\mathbf{c}}_{\mathbf{enc}} \in R^{300\times 360}$ for cycle c as input. The data is then passed through P number of parallel ABi-LSTM networks, each followed by two ReLU-activated fully connected layers, to predict the SOH of the pth previous cycle where $p = 1, 2, \dots, P$. First, the hidden state output for the pth ABi-LSTM module, $\mathbf{h}^{p}_{aB} \in R^{2d_h \times 1}$, is obtained using Eqs. (10) to (15). The predicted SOH for the pth previous cycle $c-p$ is then calculated as

$$\mathbf{h}^{p}_{aB} = f^{p}_{ABi-LSTM}\left(\mathbf{X}^{\mathbf{c}}_{\mathbf{enc}}\right) \tag{19}$$

$$\widehat{SOH}_{c-p} = ReLU\left(\mathbf{W}^{p}_{2}\left(ReLU\left(\mathbf{W}^{p}_{1}\mathbf{h}^{p}_{aB}\right)\right)\right) \tag{20}$$

where $f^{p}_{ABi-LSTM}$ refers to the pth ABi-LSTM network, $\mathbf{W}^{p}_{1} \in R^{256\times 2d_h}$, $\mathbf{W}^{p}_{2} \in R^{1\times 256}$, $\widehat{SOH}_{c-p} \in R^{1}$, and $p = 1, 2, \dots, P$. A local mean squared error (MSE) loss guides each of the P parallel networks, calculated between the predicted $\widehat{SOH}_{c-p}$ and actual SOH_{c-p} for the cycle $c-p$, during training. It is defined as

$$\mathcal{L}_{MSE}(p) = \left(\widehat{SOH}_{c-p} - SOH_{c-p}\right)^{2} \tag{21}$$

where $p = 1, 2, \dots, P$. With backpropagation from these local losses during training, the parallel networks learn to map the input data matrix for cth cycle to the past cycle SOHs, which eliminates the necessity of actual past cycle SOHs during testing.

For forecasting the SOH for cycle c from the predicted SOHs of previous P cycles, they are first concatenated to form a 2D matrix $\widehat{\mathbf{SOH}} \in R^{1\times P}$ as

$$\widehat{\mathbf{SOH}} = \left[\widehat{SOH}_{c-P} \dots \widehat{SOH}_{c-2}\ \widehat{SOH}_{c-1}\right] \tag{22}$$

This 2D matrix $\widehat{\mathbf{SOH}}$ serves as an input to an ABi-LSTM network in Fig. 5(b) such that, the total number of time steps, $T = P$ and the input at the tth time step, $\mathbf{x}_t = \widehat{SOH}_{c-P} \in R^{1\times 1}$ $(t = 1, 2, \dots, P)$. Following Eqs. (10) to (15), the output of the ABi-LSTM network can be obtained. The process can be formulated as

$$\mathbf{h}'_{aB} = f'_{ABi-LSTM}\left(\widehat{\mathbf{SOH}}\right) \tag{23}$$

where $\mathbf{h}'_{aB} \in R^{2d_{h2}\times 1}$ and d_{h2} refer to the output and the hidden state dimension of the ABi-LSTM network $f'_{ABi-LSTM}$, respectively. Since $\mathbf{h}'_{aB}$ is the final output feature from the second parallel network in Fig. 6(a), it can be represented as

$$\mathbf{h}^{2}_{\mathbf{parallel}} = \mathbf{h}'_{\mathbf{aB}} \tag{24}$$

where $\mathbf{h}^{2}_{parallel} \in R^{2d_{h2}\times 1}$.

2.4.3. Fusion network

The feature vectors $\mathbf{h}^{1}_{parallel} \in R^{2d_h\times 1}$ and $\mathbf{h}^{2}_{parallel} \in R^{2d_{h2}\times 1}$ obtained from the two parallel networks, respectively, are combined using a fusion network to output the final predicted SOH for cth cycle. Fig. 6(b) shows the schematic architecture of the fusion network where the two parallel feature vectors are first concatenated and thereafter passed through two fully connected layers to obtain the final SOH prediction. The process can be formulated as

$$\mathbf{h}^{c}_{parallel} = [\mathbf{h}^{1}_{parallel}, \mathbf{h}^{2}_{parallel}] \tag{25}$$

$$\widehat{SOH}_{c} = \mathbf{W}^{c}_{2}\left(ReLU\left(\mathbf{W}^{c}_{1}\mathbf{h}^{c}_{parallel}\right)\right) \tag{26}$$

where $h^{c}_{parallel} \in R^{2(d_h+2d_{h2})\times 1}$, $\mathbf{W}^{c}_{1} \in R^{256\times 2(d_h+d_{h2})}$, $\mathbf{W}^{c}_{2} \in R^{1\times 256}$, and $\widehat{SOH}_{c} \in R^{1}$ refer to the concatenated feature vector, weight matrices for the first and second fully connected layers, and the final predicted SOH for cycle c, respectively.

2.4.4. Real-time SOH estimation with future data reconstruction

In most recent research [6,15,33,40] and our proposed framework for SOH estimation, the input to the feature extractor network requires full charging or discharging cycle data. Therefore, for real-time prediction of the SOH at each sampling time instant during an ongoing discharging cycle, future data beyond the sampling instant to the end of that cycle is required to obtain a complete discharge cycle data. With the full cycle discharge data, the SOH then can be estimated for that particular sampling time utilizing the proposed trained network. For future data reconstruction, we followed the procedure of Qin et al. [40], the steps of which are described in the following for an ongoing discharging test cycle.

Let, for a test cycle, the input raw sensor voltage, current and temperature data are defined as $v_{test}(k)$, $i_{test}(k)$, and $t_{test}(k)$, respectively. For any sampling instant m during this test cycle, only partial discharging data $\mathbf{v}_{test}(1:m)$, $\mathbf{i}_{test}(1:m)$ and $\mathbf{t}_{test}(1:m)$ will be available. To obtain a full discharge cycle, unknown future data is required to be estimated which can be supplemented from the battery data utilized during the training by similarity checking. Let there be N number of cycles in the training dataset from a diverse set of batteries and for a particular training cycle c, the available full cycle voltage, current, and temperature data be defined as $\mathbf{v}_c(k)$, $\mathbf{i}_c(k)$ and $\mathbf{t}_c(k)$. The future data reconstruction at time step m for the test cycle is done through similarity evaluation with each of the training cycles up to this time instant. This similarity is measured by computing the Euclidean distances as defined in the following:

$$d^{v}_{c}(m) = \sqrt{\sum_{k=1}^{m}\left(\mathbf{v}_{test}(k) - \mathbf{v}_{c}(k)\right)^{2}} \tag{27}$$

$$d^{i}_{c}(m) = \sqrt{\sum_{k=1}^{m}\left(\mathbf{i}_{test}(k) - \mathbf{i}_{c}(k)\right)^{2}} \tag{28}$$

$$d^{t}_{c}(m) = \sqrt{\sum_{k=1}^{m}\left(\mathbf{t}_{test}(k) - \mathbf{t}_{c}(k)\right)^{2}} \tag{29}$$

$$d_c(m) = d^{v}_{c}(m) + d^{i}_{c}(m) + d^{t}_{c}(m) \tag{30}$$

For N sets of training cycles, N set of distances will be calculated, $D = [d_1(m), d_2(m), \dots, d_c(m), \dots, d_N(m)]$. The training cycle with the least distance, i.e., maximum similarity is chosen to construct the future data for the test cycle at sampling instant m. Let, the chosen training cycle be labeled as j with full cycle length K_j. Then the reconstructed full

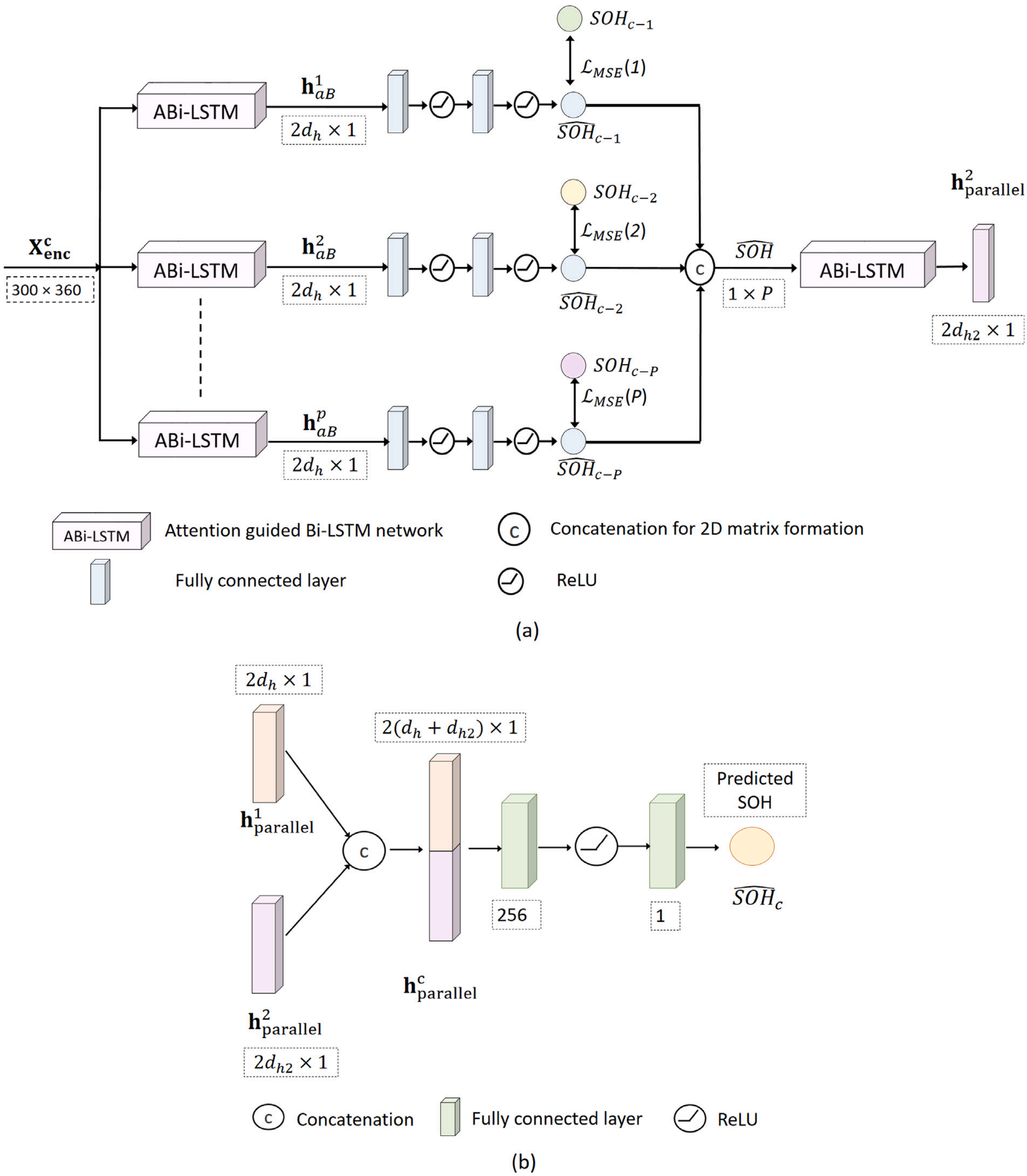

Fig. 6. (a) Architecture of the PCS-multi-ABi-LSTM network; (b) architecture of the fusion network.

cycle voltage, current, and temperature data for the test cycle at time step m is calculated as

$$\mathbf{v}^m_{test} = [\mathbf{v}_{test}(1 : m), \mathbf{v}_j(m+1 : K_j)] \tag{31}$$

$$\mathbf{i}^m_{test} = [\mathbf{i}_{test}(1 : m), \mathbf{i}_j(m+1 : K_j)] \tag{32}$$

$$\mathbf{t}^m_{test} = [\mathbf{t}_{test}(1 : m), \mathbf{t}_j(m+1 : K_j)] \tag{33}$$

The reconstructed full cycle data $\mathbf{v}^m_{test}$, $\mathbf{i}^m_{test}$, and $\mathbf{t}^m_{test}$ at sampling instant m, is preprocessed utilizing the energy discrepancy aware variable cycle length synchronization and grid encoding approach (see Fig. 4). The preprocessed data is fed to the offline well-trained proposed network to obtain the estimated SOH at time instant m, making the proposed algorithm suitable for real-time in vehicle or device SOH estimation.

2.5. Loss functions

To determine the SOH of a particular cycle, the existing deep learning-based state-of-the-art methods [6,11,15,32–35,40] utilized only a global loss based on the true SOH value of that cycle to train their network. However, in our proposed framework, instead of defining a single loss function based on the current cycle SOH, additional local losses are adopted to guide the overall feature extraction process for SOH estimation. These local losses are based on the true SOH values of the previous cycles and can provide additional guidance locally in the neural network during training. Compared to a single constraint based on the global loss, multi-objective constraints with these additional losses can aid the proposed network in extracting more effective features from the preprocessed data, improving the current cycle SOH prediction.

2.5.1. Global loss

As shown in Fig. 4, for a particular cycle c, the 2D data matrix obtained after preprocessing $\mathbf{X}^{\mathbf{c}}_{\mathbf{enc}} \in R^{300\times360}$ pass through two parallel and a fusion network to predict the battery state of health $\widehat{SOH}_c$ corresponding to this cycle. The global loss function is calculated between the predicted $\widehat{SOH}_c$ and the ground truth SOH_c to backpropagate through all three networks. It is an MSE loss computed as

$$\mathcal{L}^c_g = \left(\widehat{SOH}_c - SOH_c\right)^2 \tag{34}$$

where $\mathcal{L}^c_g$ refers to the global loss for cycle c.

2.5.2. Local loss

The local losses are calculated in the PCS-multi-ABi-LSTM network, as illustrated in Fig. 6(a). For a particular cycle, c, P number of local losses are calculated in P parallel branches, based on the predicted and ground truth SOHs of past P cycles as described in Eq. (21). The sum of these P losses represents the overall local loss which can be formulated as

$$\mathcal{L}^c_l = \sum_{p=1}^{P} \mathcal{L}_{MSE}(p) \tag{35}$$

where $\mathcal{L}^c_l$ refers to the local loss for cycle c.

2.5.3. Total loss

The total loss for the proposed framework is computed by combining the local and global loss as in the following:

$$\mathcal{L}^c = \beta\mathcal{L}^c_g + \gamma\mathcal{L}^c_l \tag{36}$$

where $\mathcal{L}^c$ refers to the total loss for cycle c. β and γ are coupling factors for the global and local losses, respectively, to be chosen appropriately. In this work, we have set $\beta = 1$ and $\gamma = 0.01$ after experimentation. Greater emphasis has been placed on the global loss since it is computed using the predicted SOH for the current cycle c compared to the local loss, which is based on the predicted SOHs of previous cycles.

2.6. Implementation and training details

All of the experiments conducted to evaluate the proposed framework have used the Kaggle Platform, which provides an NVIDIA Tesla K100 GPU with 29 GB of RAM (random-access memory). The two parallel and fusion networks in Fig. 4 are initialized with random weights which get updated with backpropagation from the global and local losses during training. For the ODS-multi-ABi-LSTM network (see Fig. 5(a)), the number of Bi-LSTM layers and the dimension of hidden state d_h in each of the parallel and series ABi-LSTM modules are set to 1 and 128, respectively. The parallel ABi-LSTM modules in the PCS-multi-ABi-LSTM (see Fig. 6(a)) also follow the same specifications except for the series ABi-LSTM module where the number of Bi-LSTM layers and the dimension of hidden state d_{h2} are set to 2 and 512, respectively. The proposed model has been trained for 100 epochs with the batch size set to 40. An adaptive moment (Adam) optimizer with an initial learning rate of 0.001 is utilized to update the model parameters. The ReduceLROnPlateau strategy is adopted for scheduling the learning rate.

To evaluate the proposed method's accuracy on diverse sets of battery data, we have employed a four-fold cross-validation approach for both individual and combined datasets. In this approach, each dataset is first split into four folds. Next, the proposed network is tested considering one fold at a time, utilizing the remaining three folds for training. During the training of each fold, the simulation data are utilized for data augmentation. With different sets of training and testing battery data, this method helps to understand the proposed framework's generalization capability.

Table 3
Performance evaluation of the proposed method with varied inputs on the combined dataset.

Input	MAPE (%)	MAE	RMSE(%)	R^2
(a) V	0.970	0.007	0.931	0.984
(b) V+ I	0.954	0.007	0.891	0.985
(c) V+ T	0.899	0.007	0.867	0.986
(d) V+ I+ T (Proposed Method)	**0.754**	**0.005**	**0.680**	**0.992**

2.7. Performance evaluation metrics

Four common quantitative performance metrics are utilized to assess the performance of the proposed approach for SOH estimation: mean absolute error (MAE), mean absolute percentage error (MAPE), root mean square error (RMSE), and coefficient of determination (R^2). These metrics can be calculated as in the following:

$$\text{MAE} = \frac{1}{C}\sum_{c=1}^{C}\left|SOH_c - \widehat{SOH}_c\right| \tag{37}$$

$$\text{MAPE} = \frac{1}{C}\sum_{c=1}^{C}\frac{\left|SOH_c - \widehat{SOH}_c\right|}{SOH_c} \times 100\% \tag{38}$$

$$\text{RMSE} = \sqrt{\frac{1}{C}\sum_{c=1}^{C}\left(SOH_c - \widehat{SOH}_c\right)^2} \times 100\% \tag{39}$$

$$\text{R}^2 = 1 - \frac{\sum_{c=1}^{C}\left(SOH_c - \widehat{SOH}_c\right)^2}{\sum_{c=1}^{C}\left(SOH_c - \overline{SOH}\right)^2} \tag{40}$$

where C denotes the total number of cycles in the test battery. SOH_c and $\widehat{SOH}_c$ refer to the actual and predicted SOH, respectively, for cycle c, and $\overline{SOH}$ refers to the mean of the actual SOH values of C cycles.

3. Experimental results and discussion

In this section, experiments are conducted on four publicly available datasets and a combination of these four datasets referred to as the combined dataset to evaluate the performance of the proposed framework for battery SOH estimation. The selection of different components in the framework is validated by demonstrating the influence of varying input battery data, the advantage of the data preprocessing scheme, the effect model architecture, i.e., selection of the base model, attention mechanism, parallel modular components and loss functions, and the effect of data augmentation with simulation data. Finally, the performance of the proposed method is compared with other state-of-the-art methods [26,40]. These experiments are conducted with full cycle discharge data as input. Additionally, the real-time SOH estimation performance of the proposed framework, i.e., SOH estimation at each sampling time during an ongoing discharge cycle with partial discharge data instead of at the end of the full discharge cycle, is also presented along with a comparison with another state-of-the-art method [40].

3.1. Influence of varying input data

Recent research on deep learning-based SOH estimation algorithms utilized raw sensor data [6,15,33,34,40] such as, voltage (V), current (I), and temperature (T) or processed data from the raw V and I such as discharging capacity vs. voltage curve [35], IC curve [35], differential current curves [11], differential voltage curve [32], and capacity changing curve [11] as input to the automatic feature extraction network. However, in the proposed framework, only raw sensor

Table 4
Performance evaluation of the proposed method with different preprocessing schemes on the combined dataset.

Preprocessing Method	MAPE (%)	MAE	RMSE(%)	R^2
(a) ICS	6.272	0.049	5.773	0.423
(b) EDVCS	0.960	0.006	0.741	0.990
(c) EDVCS+ GE (Proposed Method)	**0.754**	**0.005**	**0.680**	**0.992**

Table 5
Performance evaluation of different RNN models on the combined dataset.

Models	MAPE (%)	MAE	RMSE(%)	R^2
GRU	1.584	0.009	1.263	0.970
LSTM	1.475	0.008	1.178	0.980
Bi-LSTM	1.220	0.007	0.985	0.985

data has been used as input to avoid the additional computational cost of processing the data. Different combinations of V, I, and T data have been fed as inputs to the proposed network to observe input variation's effect on SOH estimation, summarized in Table 3 for the combined dataset. It can be observed that the combination of all three sensor data V, I, and T provide superior SOH estimation results with 0.754% MAPE, 0.005 MAE, 0.680% RMSE, and 0.992 R^2. Since the battery cells of the four datasets discharge with different C-rated currents and operating temperatures, including I and T inputs can model the effect of discharging current and temperature variation on battery health degradation, providing complementary information to raw voltage data, and therefore obtains better SOH estimation results on the combined dataset. This is proved by the gradual improvement in SOH estimation accuracy from (a) to (d) in Table 3, specifically 0.216%, 0.002, and 0.251% decrease in MAPE, MAE and RMSE, respectively, 0.008 increase in R^2 with the combined input V, I and T compared to V data alone.

3.2. Effect of the data preprocessing scheme

In our proposed framework, the raw sensor data are preprocessed in two steps: (i) Energy discrepancy aware variable cycle length synchronization (EDVCS) and (ii) Grid encoding (GE). To show the effect of the proposed synchronization approach, EDVCS, an interpolation-based cycle length synchronization (ICS) method is applied where the variable lengthed cycle data, due to the increase in cycle number or variation in discharge current rates, are synchronized to a fixed length 360 (same as the EDVCS) using the 'cubic spline' interpolation approach. From the results presented in Table 4, it can be observed that the ICS preprocessing approach shows subpar performance on the combined dataset with 6.272% MAPE, 0.049 MAE, 5.773% RMSE and 0.423 R^2. This is expected because, without the energy discrepancy constraints, the discrepancies across the cycled data with the increase of battery health degradation are scaled down after interpolation-based cycle length synchronization. In addition, the variation in cycle length due to variation in discharging current rates despite the same SOH is not handled properly in this method. This is another reason for lower performance in the combined dataset where battery cells with varied discharging current rates are present. In the first preprocessing step of the proposed framework, EDVCS, both of these issues are considered, as discussed in Section 2.3.1 showing a great improvement in SOH estimation performance. As can be observed from Table 4 (b), the EDVCS approach outperforms the ICS in (a) by 5.312%, 0.043, 5.032% decrease in MAPE, MAE and RMSE, respectively, and a 0.567 increase in R^2 value. The addition of the second preprocessing step, GE, further improves the SOH estimation performance with 0.21%, 0.043, and 0.061% decreases in MAPE, MAE and RMSE, respectively. These results prove that our grid encoding scheme effectively increases the minor discrepancies within the cycled data of varied states of health and helps the proposed network to effectively model the cycling data of different batteries with different specifications, in the combined dataset, to their corresponding SOHs, thus obtaining generalizability.

3.3. Effect of the model architecture

3.3.1. Impact of base model selection

As shown in Fig. 4, the basis of the proposed architecture is the ABi-LSTM network. The selection of this Bi-LSTM network was based on the performance comparison with other RNN models such as GRU and LSTM, as presented in Table 5, demonstrating the efficacy in modeling the time series preprocessed discharge battery data and mapping them into battery SOH. From Table 5 it can be observed that the Bi-LSTM model outperforms GRU and LSTM with 1.220% MAPE, 0.007% MAE, 0.985% RMSE and 0.985 R^2. As discussed in Section 2.4.1, compared to LSTM and GRU, the Bi-LSTM model can better capture the dependencies in the input sequential data by processing it in both forward and backward directions providing better SOH estimation. Hence it is selected as the base model in the proposed architecture.

3.3.2. Impact of attention mechanism

After the data preprocessing step, the sampled voltage, current and temperature data over increasing cycles achieve synchronized lengths (360 in this paper). However, hidden state features extracted from these data by the Bi-LSTM network at each of the sampling times, ranging from 1 to 360, may not be equally important for battery health prediction. The sampling times, at which these battery data largely vary over the cycles, can better model the relation between the cycle-varying data and the corresponding SOH and contribute more to the SOH estimation. The temporal attention mechanism in this work is employed on the hidden state features of the Bi-LSTM network such that the features from the more important sampling times are assigned higher weights compared to the less important ones, dynamically, during the training of the network. As shown in Table 6, ABi-LSTM achieves a 0.198%, 0.001, and 0.201% decrease in MAPE, MAE and RMSE, respectively, and a 0.006 increase in the R^2 value compared to the base Bi-LSTM network. This substantiates that the attention mechanism can improve the performance of SOH estimation. Hence, ABi-LSTM is selected as the core network in the proposed framework in Fig. 4.

3.3.3. Impact of ODS-multi-ABi-LSTM

The ODS-multi-ABi-LSTM is employed to further improve the performance of the ABi-LSTM network. As shown in Table 6, the ODS-multi-ABi-LSTM network provides better SOH prediction with 0.892% MAPE, 0.006 MAE, 0.715% RMSE, and 0.992 R^2 compared to a single ABi-LSTM. This network extracts features from the preprocessed data by splitting it into overlapping time segments through multiple parallel ABi-LSTM networks which facilitates efficient feature extraction from shorter data segments and better learning of the dependencies within a particular sequence in comparison to a single ABi-LSTM network with full cycle length data (1 to 360) as input.

3.3.4. Impact of PCS-multi-ABi-LSTM

The PCS-multi-ABi-LSTM shows the impact of a time-series forecasting approach on SOH estimation accuracy compared to direct SOH estimation through a single ABi-LSTM network. As can be observed from Table 6, this approach achieves a 0.11% and 0.018% decrease in MAPE and RMSE, respectively over the ABi-LSTM network. This network, with parallel ABi-LSTM networks for predicting previous cycles' SOHs followed by another ABi-LSTM for forecasting them into current cycle SOH prediction, is guided by both local and global losses in an end-to-end training manner (as shown in Fig. 6(a)). Utilization of multiple loss functions enforces better feature learning from the preprocessed data. Therefore, in comparison to a single ABi-LSTM network trained with only the global loss based on the true value of the current cycle SOH, the PCS-multi-ABi-LSTM provides better SOH estimation.

Table 6
Ablation experiment showing the effect of multiple parallel modules in the proposed framework using the combined dataset.

Model	MAPE (%)	MAE	RMSE(%)	R^2
(a) Bi-LSTM	1.220	0.007	0.985	0.985
(b) ABi-LSTM	1.022	0.006	0.784	0.991
(c) ODS-multi-ABi-LSTM	0.892	0.006	0.716	0.992
(d) PCS-multi-ABi-LSTM	0.912	0.006	0.766	0.991
(e) c + d + FN (Proposed Method)	0.754	0.005	0.680	0.992
(f) e + simulation data augmentation	**0.716**	**0.005**	**0.653**	**0.992**

Table 7
Performance comparison among different models on NASA dataset.

Method	MAPE (%)	MAE	RMSE(%)	R^2
Li et al. [26]	4.292	0.033	3.689	0.839
Qin et. al [40]	2.358	0.017	2.431	0.905
Wang et al. [36]	2.532	0.019	2.091	0.941
Proposed Method	**0.921**	**0.007**	**0.807**	**0.991**

Table 8
Performance comparison among different models on Oxford dataset.

Method	MAPE (%)	MAE	RMSE(%)	R^2
Li et al. [26]	2.629	0.023	2.686	0.783
Qin et. al [40]	1.097	0.009	1.517	0.932
Wang et al. [36]	2.031	0.017	1.853	0.913
Proposed Method	**0.272**	**0.002**	**0.440**	**0.994**

3.3.5. Impact of FN

The addition of a fusion network combining the features of ODS-multi-ABi-LSTM and PCS-multi-Bi-LSTM, as in the proposed architecture (see Fig. 4), provides superior performance to individual ODS-multi-ABi-LSTM and PCS-multi-ABi-LSTM networks. As shown in Table 6, the proposed method predicts battery SOH with 0.754% MAPE, 0.005 MAE, 0.680% RMSE, and 0.992 R^2 values on the combined dataset. This indicates a decrease of 0.138%, 0.001, 0.036% in MAPE, MAE and RMSE, respectively, compared to the ODS-multi-ABi-LSTM network alone and a decrease of 0.158%, 0.001, 0.086% in MAPE, MAE and RMSE, respectively, compared to the PCS-multi-ABi-LSTM network. The better SOH estimation results indicate efficient feature mixing in the fusion network through concatenating the extracted features of the ODS-multi-ABi-LSTM and PCS-multi-ABi-LSTM network and then passing them through two fully connected layers.

3.4. Effect of data augmentation with simulation data

In the preceding subsections, the effect of varying input data, data preprocessing technique, and model architecture were demonstrated utilizing solely the experimental datasets (NASA, Oxford, MIT, CALCE) to discretely show the influence of data augmentation during training. As can be observed from Table 6, with the addition of simulation data, our proposed method achieves 0.716% MAPE, 0.005% MAE, 0.653% RMSE and 0.992 R^2 value on the combined dataset. This indicates a 0.038% and 0.027% decrease in MAPE and RMSE, respectively over the proposed method trained with only experimental data. The augmentation with simulation data of a distinct battery cell under different operating conditions further enhances our model's learning during training. Incorporating additional data, the model can extract more generalized features that reflect the relationship between diverse voltage, current, and temperature data under diverse operating conditions and the resulting change in battery health deterioration patterns, thereby improving the overall accuracy of battery SOH prediction.

3.5. Comparison with other methods

The SOH estimation performance of the proposed framework is compared with three existing state-of-the-art methods on the four

Table 9
Performance comparison among different models on MIT dataset.

Method	MAPE (%)	MAE	RMSE(%)	R^2
Li et al. [26]	1.034	0.009	1.165	0.951
Qin et. al [40]	0.665	0.006	0.728	0.981
Wang et al. [36]	0.682	0.006	0.765	0.981
Proposed Method	**0.557**	**0.005**	**0.604**	**0.988**

Table 10
Performance comparison among different models on CALCE dataset.

Method	MAPE (%)	MAE	RMSE(%)	R^2
Li et al. [26]	8.660	0.061	6.494	0.859
Qin et al. [40]	2.237	0.009	1.946	0.984
Wang et al. [36]	3.205	0.018	2.156	0.987
Proposed Method	**1.480**	**0.006**	**0.962**	**0.995**

Table 11
Performance comparison among different models on Combined dataset.

Method	MAPE (%)	MAE	RMSE(%)	R^2
Li et al. [26]	9.945	0.076	8.631	−0.619
Qin et al. [40]	2.397	0.018	2.525	0.767
Wang et al. [36]	1.861	0.014	1.581	0.953
Proposed Method	**0.716**	**0.005**	**0.653**	**0.992**

publicly available datasets individually and on the combined dataset. The four-fold cross-validation results are presented in Tables 7–11. For each of the datasets, our method outperforms other methods across all evaluation metrics. In addition, Figs. 8–11 plots the SOH prediction results of the proposed and the other three methods for four cells from each dataset. Li et al. [26] employed a linear regression-based machine-learning algorithm for predicting battery health status where the DVW distance between the IC curves of the current and initial cycle of a particular battery was calculated as the health-indicating feature. The linear relationship between the extracted features and the corresponding SOH was enhanced by the box-cox transformation method and finally, a linear regression model was fit across the training data. Like most machine learning algorithms, their method suffers from optimum feature selection and generalizability problems. The fitted linear model is biased towards the training data and achieves low SOH estimation accuracy for unknown battery data. Among all of the datasets, this method performs comparatively better on the Oxford (see Table 8) and MIT datasets (see Table 9) since the battery cells in this dataset have similar discharging profiles. However, with the handcrafted feature as input the linear model cannot be effectively fit across battery cells with varying discharging profiles and hence obtains low SOH estimation accuracy on the NASA (see Table 7), CALCE (see Table 10) and the combined dataset (see Table 11). Qin et al. [40] employed a deep learning-based algorithm for automatic feature extraction from discharging voltage, and temperature data and achieves superior performance to the previous machine learning-based approach (see Tables 7–11). An energy discrepancy aware time warping approach and grid encoding were adopted as the preprocessing scheme and the preprocessed data was fed to a time attention based Bi-LSTM model for mapping to the corresponding SOH. However, since their method was evaluated across a single dataset, their preprocessing scheme did not take into account the cases of multiple battery cells with varying discharging profiles. In addition, in their time attention approach, a fixed discharging time interval was selected based on the training data and other samples of that discharging cycle were discarded. This fixed discharging time interval may not provide optimum results for any unknown test battery data with different specifications. Wang et al. [36] implemented an explainable deep learning based algorithm based on LSTM and CNN network to automatically extract features from voltage, current, and temperature data. Though their method is

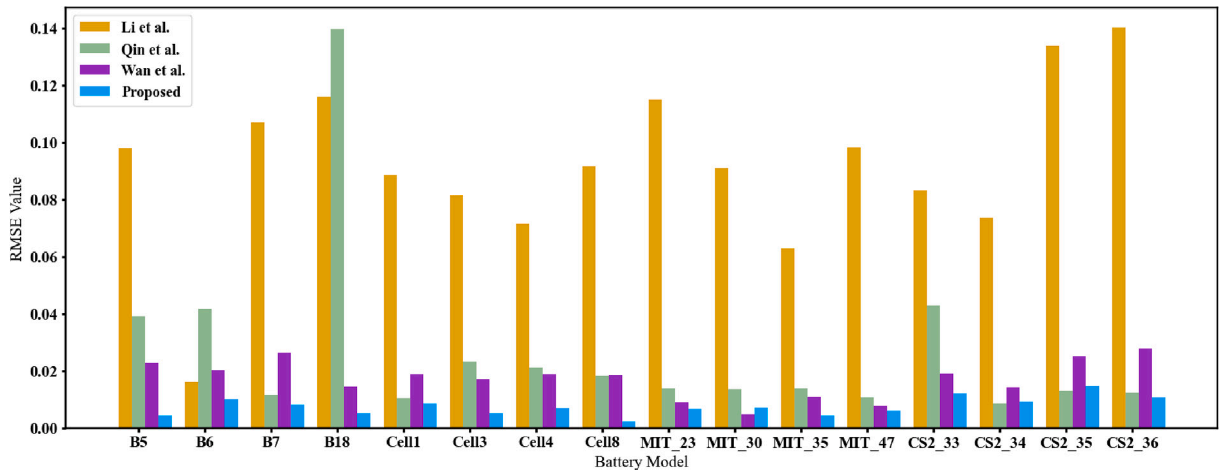

Fig. 7. Bar plot of RMSE for different methods on sixteen different battery models from four datasets (NASA, Oxford, MIT, and CALCE).

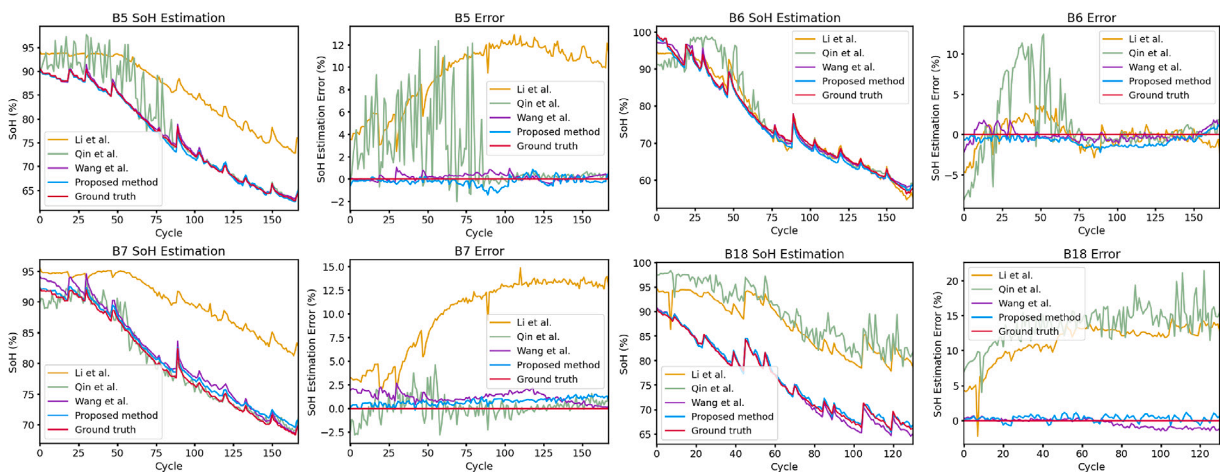

Fig. 8. SOH estimation performance comparison of the proposed method with other methods on NASA dataset.

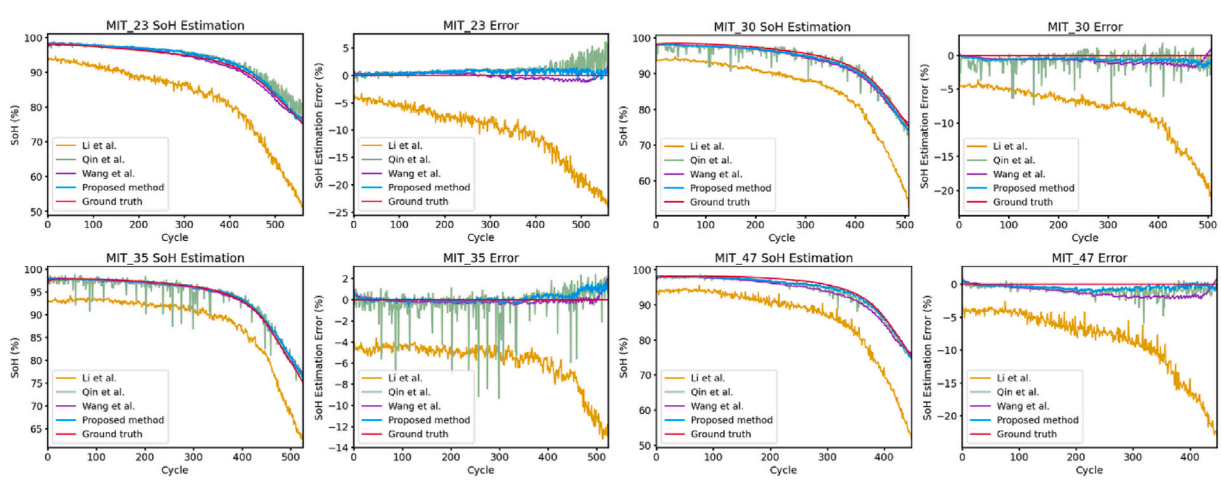

Fig. 9. SOH estimation performance comparison of the proposed method with other methods on MIT dataset.

outperformed by the works of Qin et al. on four individual datasets (see Tables 7–10), it outperforms other two state-of-the-art methods on the combined dataset (see Table 11).

In contrast to the works of Qin et al. [40], our preprocessing scheme can handle battery cells with diverse discharge profiles. The temporal attention module in the proposed network assigns weights for the discharging sampling times according to their importance during training without completely discarding any of the samples. Furthermore, instead of using a single LSTM network, our approach explores the possibility of variations and series-parallel combinations of multiple LSTM networks. Our proposed overlapped data splitting allows the Bi-LSTM network to captures enhanced temporal context while increasing

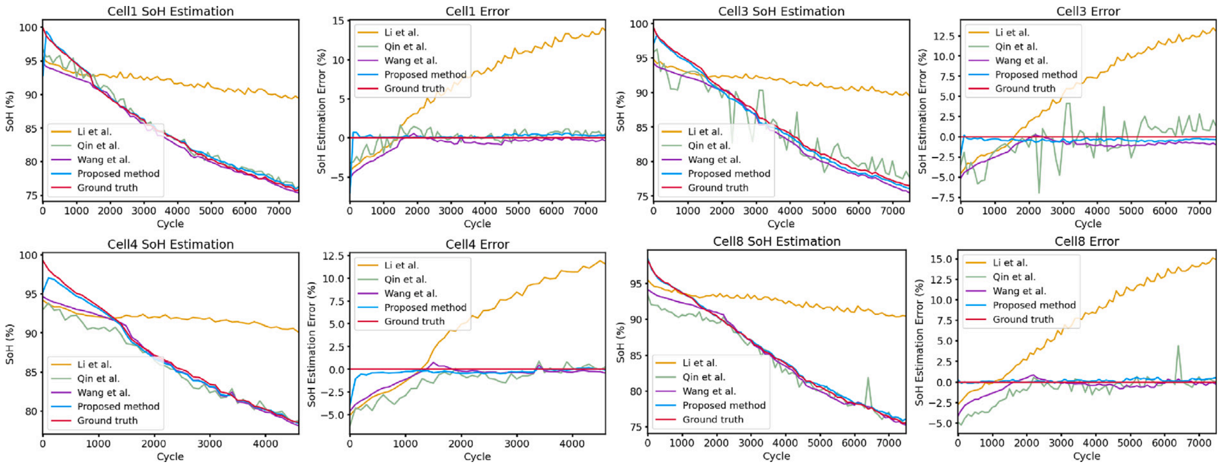

Fig. 10. SOH estimation performance comparison of the proposed method with other methods on Oxford dataset.

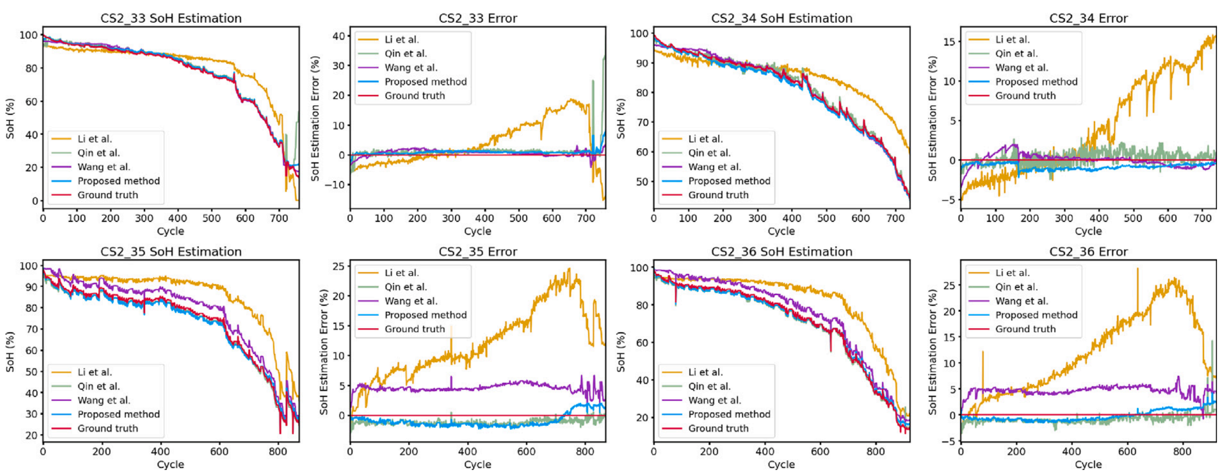

Fig. 11. SOH estimation performance comparison of the proposed method with other methods on CALCE dataset.

data diversity. From Tables 7–11, it can be observed that our method outperforms the best-comparing technique, Qin et al. [40] in all four individual datasets and achieves a 1.681%, 0.013, and 1.872% decrease in MAPE, MAE and RMSE, respectively, and 0.225 increase in R^2 value for the combined dataset. However, it should be noted that while implementing the method of Qin et al. [40], our preprocessing scheme has been adapted since the preprocessing equations presented in their paper contained possible errors regarding matrix dimensions mismatch and could not be implemented. Nevertheless, despite using the same preprocessing technique, the proposed method yields the best SOH estimation performance with its novel parallel architecture and fusion mechanism in place of a single LSTM network and augmentation of training data via the presented battery simulation model.

The bar plot in Fig. 7 illustrates the superior performance of the proposed method across various battery models compared to other state-of-the-art methods. Excluding the MIT_30 battery cell, the proposed method achieves a notably lower RMSE on all battery cells. The efficacy of the proposed technique is also evident from the SOH (%) vs cycle plots and the corresponding error (%) plots in Figs. 8–11. Compared to Li et al. [26], Qin et al. [40], and Wang et al. [36], our SOH (%) prediction curves are smoother, have less randomness and are closer to the ground truth values.

3.6. Real-time SOH estimation

The SOH estimation performance presented in Tables 7–11 and Figs. 8–11 are end of discharging cycle SOH estimation. However, for real-life applications of lithium-ion batteries, battery health status is predicted using the proposed method at each sampling time of an ongoing discharging cycle by utilizing the future data reconstruction technique described in Section 2.4.4. The results are presented in Fig. 12(a)–(d) and compared with the technique of Qin et al. [40].

From the plots (Fig. 12(a)–(d)), it can be observed that for each cycle, SOH estimation errors are higher for the initial sampling times and gradually decrease towards the end of the cycle. This is more evident from Fig. 12(e)–(h), where error distribution over all cycles (up to the end of life) at different sampling times for four battery cells, one from each dataset, is presented. The median RMSE error, represented with the 'o' sign, decreases with the increase in time. At the initial sampling times, the reconstructed full cycle contains less of the real-valued samples and more of the reconstructed samples, yielding low SOH estimation accuracy. However, after a certain time ($101th$ sampling instant in Fig. 12(e)–(h)), the RMSE error remains under a considerable margin, 0 to 5%, for the proposed method. For both Fig. 12(a)–(d) and (e)–(h), the true SOH value at the end of the corresponding discharging cycle is considered the ground truth. Although the same data reconstruction technique and preprocessing approach have been applied for both Qin et al. [40] and the proposed method, our predicted SOHs are closer to the ground truth value at each sampling time, as demonstrated in Fig. 12(a)–(d). These results further verify the efficacy of the parallel modules, multiple loss functions and data augmentation technique in the proposed network architecture for higher battery health status prediction accuracy.

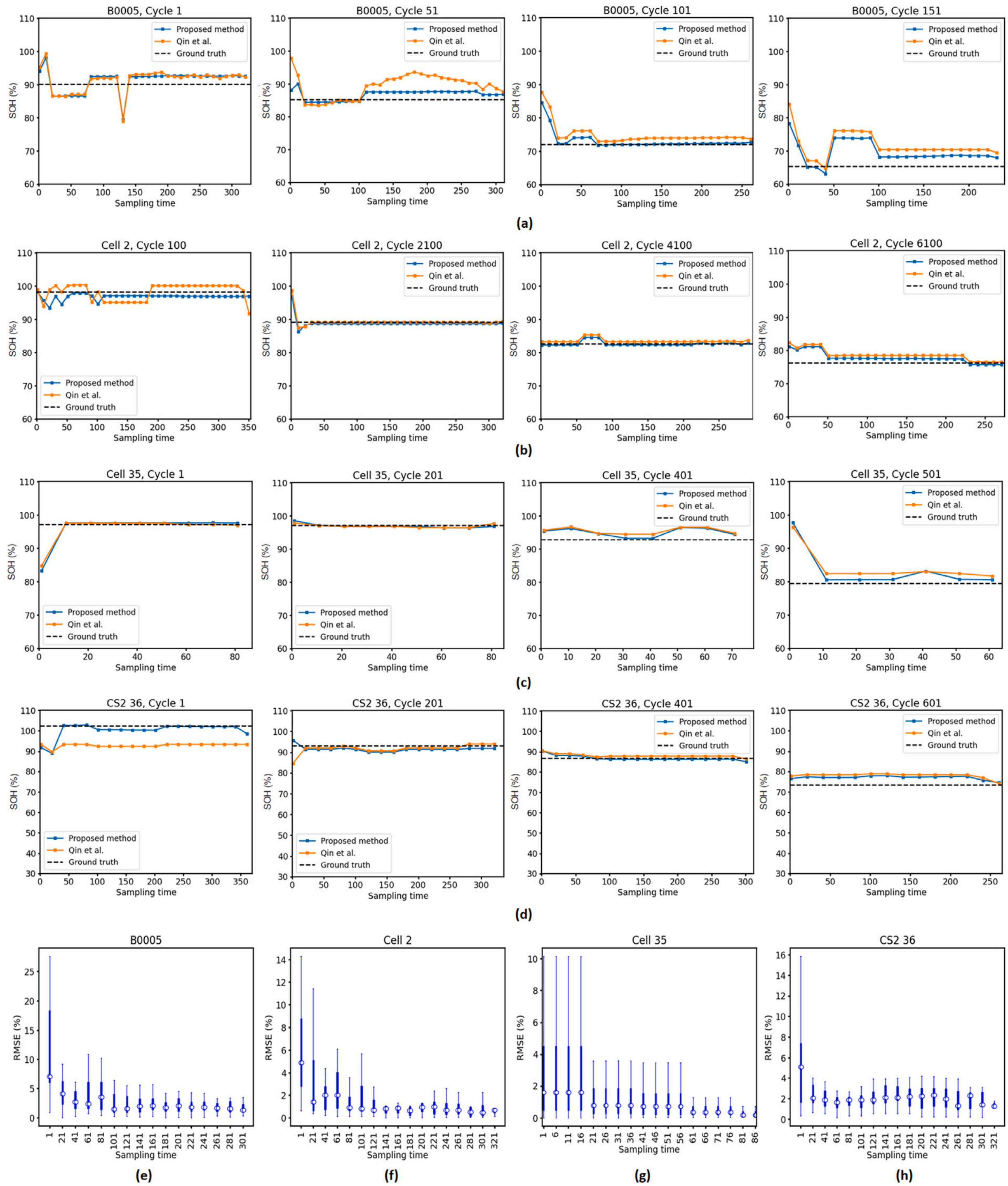

Fig. 12. Real-time SOH estimation performance of the proposed method with increasing cycle numbers for battery cells: (a) B0005 (NASA dataset); (b) Cell 2 (Oxford dataset); (c) Cell 35 (MIT dataset); (d) CS2 36 (CALCE dataset), error distribution over all cycles at different sampling times for battery cells: (a) B0005 (NASA dataset); (b) Cell 2 (Oxford dataset); (c) Cell 35 (MIT dataset); (d) CS2 36 (CALCE dataset).

4. Conclusion

This paper has proposed a novel framework for real-time SOH estimation of lithium-ion batteries, emphasizing high accuracy and generalization across diverse battery sets. The framework includes a unique preprocessing scheme that incorporates energy discrepancy-aware cycle length synchronization and grid encoding, normalizing data from varied battery cells with differing discharge profiles and temperatures to create a standardized input. Unlike typical deep learning approaches that rely on a single RNN or CNN architecture, the proposed framework employs two parallel networks – ODS-multi-ABi-LSTM and PCS-multi-ABi-LSTM – to extract complementary features for SOH estimation. These features are then integrated using a fusion network. It has been demonstrated that the use of multi-objective loss functions, comprising global and local losses, can further enhance the SOH prediction accuracy. Additionally, simulation-based data augmentation enriches the training dataset, promoting more generalized feature learning and improved SOH estimation performance. The framework's efficacy is demonstrated through superior performance across all evaluation metrics, surpassing state-of-the-art techniques on four distinct and combined datasets. However, for real-time SOH estimation, the adopted future data reconstruction algorithm assumes that the discharging cycle starts from a fully charged condition of the battery which may not be the case in many practical applications. Also, real-world applications exhibit extremely fluctuating currents due to dynamic driving patterns which is not the case for available four datasets. Future work will address these limitations by incorporating flexible cycle start points. Enhanced techniques to simulate full discharge cycles and adaptive filters for fluctuating currents may also be explored to accommodate real-world driving patterns and improve SOH estimation robustness.

CRediT authorship contribution statement

Jarin Tasnim: Writing – original draft, review & editing, Methodology, Visualization, Investigation, Formal Analysis. **Md. Azizur Rahman:** Methodology, Data Curation. **Md. Shoaib Akhter Rafi:** Validation, Visualization, Writing – review & editing. **Muhammad Anisuzzaman Talukder:** Resources, Project Administration, Funding Acquisition, Conceptualization, Writing – review & editing. **Md. Kamrul Hasan:** Supervision, Resources, Project Administration, Funding Acquisition, Conceptualization, Methodology, Formal Analysis, Writing – review & editing.

Declaration of competing interest

The authors declare the following financial interests/personal relationships which may be considered as potential competing interests: The authors declare that they have no known competing financial interests or personal relationships that could have appeared to influence the work reported in this paper.

Acknowledgment

This research is carried out with the financial support (RISE/MoU/Poly Cable Ind/2021-02) received from Poly Cables Industries Limited, Bangladesh.

Data availability

Data will be made available on request.

References

[1] X. Hu, C. Zou, C. Zhang, Y. Li, Technological developments in batteries: A survey of principal roles, types, and management needs, IEEE Power Energy Mag. 15 (5) (2017) 20–31.
[2] Y. Li, K. Liu, A.M. Foley, A. Zülke, M. Berecibar, E. Nanini-Maury, J. Van Mierlo, H.E. Hoster, Data-driven health estimation and lifetime prediction of lithium-ion batteries: A review, Renew. Sustain. Energy Rev. 113 (2019) 109254.
[3] K. Liu, K. Li, Q. Peng, C. Zhang, A brief review on key technologies in the battery management system of electric vehicles, Front. Mech. Eng. 14 (1) (2018) 47–64.
[4] S.M. Rezvanizaniani, Z. Liu, Y. Chen, J. Lee, Review and recent advances in battery health monitoring and prognostics technologies for electric vehicle (EV) safety and mobility, J. Power Sources 256 (2014) 110–124.
[5] Y. Ma, C. Shan, J. Gao, H. Chen, Multiple health indicators fusion-based health prognostic for lithium-ion battery using transfer learning and hybrid deep learning method, Reliab. Eng. Syst. Saf. 229 (2023) 108818.
[6] Y. Fan, F. Xiao, C. Li, G. Yang, X. Tang, A novel deep learning framework for state of health estimation of lithium-ion battery, J. Energy Storage 32 (2020) 101741.
[7] Y. Zhou, M. Huang, Y. Chen, Y. Tao, A novel health indicator for on-line lithium-ion batteries remaining useful life prediction, J. Power Sources 321 (2016) 1–10.
[8] C. Pastor-Fernandez, W. Dhammika Widanage, J. Marco, M.-A. Gama-Valdez, G.H. Chouchelamane, Identification and quantification of aging mechanisms in lithium-ion batteries using the EIS technique, in: 2016 IEEE Transportation Electrification Conference and Expo, ITEC, IEEE, 2016.
[9] J. Li, K. Adewuyi, N. Lotfi, R. Landers, J. Park, A single particle model with chemical/mechanical degradation physics for lithium ion battery state of health (SOH) estimation, Appl. Energy 212 (2018) 1178–1190.
[10] S. Atalay, M. Sheikh, A. Mariani, Y. Merla, E. Bower, W.D. Widanage, Theory of battery aging in a lithium-ion battery: Capacity fade, nonlinear aging and lifetime prediction, J. Power Sources 478 (2020) 229026.
[11] S.-Z. Chen, Z. Liang, H. Yuan, L. Yang, F. Xu, Y. Fan, A novel state of health estimation method for lithium-ion batteries based on constant-voltage charging partial data and convolutional neural network, Energy 283 (2023) 129103.
[12] G.L. Plett, Extended Kalman filtering for battery management systems of LiPB-based HEV battery packs, J. Power Sources 134 (2) (2004) 262–276.
[13] L. Ma, Y. Xu, H. Zhang, F. Yang, X. Wang, C. Li, Co-estimation of state of charge and state of health for lithium-ion batteries based on fractional-order model with multi-innovations unscented Kalman filter method, J. Energy Storage 52 (2022) 104904.
[14] S. Amir, M. Gulzar, M.O. Tarar, I.H. Naqvi, N.A. Zaffar, M.G. Pecht, Dynamic equivalent circuit model to estimate state-of-health of lithium-ion batteries, IEEE Access 10 (2022) 18279–18288.
[15] S. Bockrath, V. Lorentz, M. Pruckner, State of health estimation of lithium-ion batteries with a temporal convolutional neural network using partial load profiles, Appl. Energy 329 (2023) 120307.
[16] G. Liu, X. Zhang, Z. Liu, State of health estimation of power batteries based on multi-feature fusion models using stacking algorithm, Energy 259 (2022) 124851.
[17] M. Lin, C. Yan, J. Meng, W. Wang, J. Wu, Lithium-ion batteries health prognosis via differential thermal capacity with simulated annealing and support vector regression, Energy 250 (2022) 123829.
[18] D. Yang, X. Zhang, R. Pan, Y. Wang, Z. Chen, A novel Gaussian process regression model for state-of-health estimation of lithium-ion battery using charging curve, J. Power Sources 384 (2018) 387–395.
[19] H. Jin, N. Cui, L. Cai, J. Meng, J. Li, J. Peng, X. Zhao, State-of-health estimation for lithium-ion batteries with hierarchical feature construction and auto-configurable Gaussian process regression, Energy 262 (2023) 125503.
[20] X. Zhu, W. Wang, G. Zou, C. Zhou, H. Zou, State of health estimation of lithium-ion battery by removing model redundancy through aging mechanism, J. Energy Storage 52 (2022) 105018.
[21] X. Shu, J. Shen, G. Li, Y. Zhang, Z. Chen, Y. Liu, A flexible state-of-health prediction scheme for lithium-ion battery packs with long short-term memory network and transfer learning, IEEE Trans. Transp. Electrif. 7 (4) (2021) 2238–2248.
[22] H. Ruan, H. He, Z. Wei, Z. Quan, Y. Li, State of Health Estimation of Lithium-Ion Battery Based on Constant-Voltage Charging Reconstruction, IEEE J. Emerg. Sel. Top. Power Electron. 11 (4) (2023) 4393–4402.
[23] Y. Li, M. Abdel-Monem, R. Gopalakrishnan, M. Berecibar, E. Nanini-Maury, N. Omar, P. van den Bossche, J. Van Mierlo, A quick on-line state of health estimation method for li-ion battery with incremental capacity curves processed by Gaussian filter, J. Power Sources 373 (2018) 40–53.
[24] X. Li, C. Yuan, Z. Wang, State of health estimation for li-ion battery via partial incremental capacity analysis based on support vector regression, Energy 203 (2020) 117852.
[25] S. Zhang, B. Zhai, X. Guo, K. Wang, N. Peng, X. Zhang, Synchronous estimation of state of health and remaining useful lifetime for lithium-ion battery using the incremental capacity and artificial neural networks, J. Energy Storage 26 (2019) 100951.
[26] L. Li, Y. Li, W. Cui, Z. Chen, D. Wang, B. Zhou, D. Hong, A novel health indicator for online health estimation of lithium-ion batteries using partial incremental capacity and dynamic voltage warping, J. Power Sources 545 (2022) 231961.
[27] N. Yang, Z. Song, H. Hofmann, J. Sun, Robust state of health estimation of lithium-ion batteries using convolutional neural network and random forest, J. Energy Storage 48 (2022) 103857.
[28] C.N. Van, D.T. Quang, Estimation of SOH and internal resistances of lithium ion battery based on LSTM network, Int. J. Electrochem. Sci. 18 (6) (2023) 100166.
[29] P. Jiang, T. Zhang, G. Huang, W. Hua, Y. Zhang, W. Wang, T. Zhu, An end-cloud collaboration approach for state-of-health estimation of lithium-ion batteries based on bi-LSTM with collaboration of multi-feature and attention mechanism, Int. J. Green Energy (2024) 1–13.
[30] H. Sun, J. Sun, K. Zhao, L. Wang, K. Wang, Data-driven ICA-bi-LSTM-combined lithium battery SOH estimation, Math. Probl. Eng. 2022 (1) (2022) 9645892.
[31] W. Wang, G. Yang, M. Li, Z. Yan, L. Zhang, H. Yu, K. Yang, P. Jiang, W. Hua, Y. Zhang, et al., State-of-health estimation for lithium-ion batteries based on Bi-LSTM-AM and LLE feature extraction, Front. Energy Res. 11 (2023) 1205165.
[32] C. Qian, B. Xu, L. Chang, B. Sun, Q. Feng, D. Yang, Y. Ren, Z. Wang, Convolutional neural network based capacity estimation using random segments of the charging curves for lithium-ion batteries, Energy 227 (2021) 120333.
[33] Y. Choi, S. Ryu, K. Park, H. Kim, Machine learning-based lithium-ion battery capacity estimation exploiting multi-channel charging profiles, IEEE Access 7 (2019) 75143–75152.
[34] S. Shen, M. Sadoughi, M. Li, Z. Wang, C. Hu, Deep convolutional neural networks with ensemble learning and transfer learning for capacity estimation of lithium-ion batteries, Appl. Energy 260 (2020) 114296.
[35] Z. Lu, Z. Fei, B. Wang, F. Yang, A feature fusion-based convolutional neural network for battery state-of-health estimation with mining of partial voltage curve, Energy 288 (2024) 129690.

[36] F. Wang, Z. Zhao, Z. Zhai, Z. Shang, R. Yan, X. Chen, Explainability-driven model improvement for SOH estimation of lithium-ion battery, Reliab. Eng. Syst. Saf. 232 (2023) 109046.
[37] S. Arbaoui, A. Samet, A. Ayadi, T. Mesbahi, R. Boné, Data-driven strategy for state of health prediction and anomaly detection in lithium-ion batteries, Energy AI 17 (2024) 100413.
[38] J. Gao, D. Yang, S. Wang, Z. Li, L. Wang, K. Wang, State of health estimation of lithium-ion batteries based on mixers-bidirectional temporal convolutional neural network, J. Energy Storage 73 (2023) 109248.
[39] M.K. Khan, M.A. Houran, K. Kauhaniemi, M.H. Zafar, M. Mansoor, S. Rashid, Efficient state of charge estimation of lithium-ion batteries in electric vehicles using evolutionary intelligence-assisted GLA–CNN–Bi-LSTM deep learning model, Heliyon 10 (15) (2024) e35183.
[40] Y. Qin, A. Arunan, C. Yuen, Digital twin for real-time li-ion battery state of health estimation with partially discharged cycling data, IEEE Trans. Ind. Informat. 19 (5) (2023) 7247–7257.
[41] B. Saha, K. Goebel, Battery data set, NASA AMES Prognost. Data Reposit. (2007).
[42] C. Birkl, Oxford Battery Degradation Dataset 1, University of Oxford, 2017.
[43] K.A. Severson, P.M. Attia, N. Jin, N. Perkins, B. Jiang, Z. Yang, M.H. Chen, M. Aykol, P.K. Herring, D. Fraggedakis, et al., Data-driven prediction of battery cycle life before capacity degradation, Nat. Energy 4 (5) (2019) 383–391.
[44] N. Williard, W. He, M. Osterman, M. Pecht, Comparative analysis of features for determining state of health in lithium-ion batteries, Int. J. Prognost. Health Manag. 4 (1) (2020).
[45] S.N. Motapon, A. Lupien-Bedard, L.-A. Dessaint, H. Fortin-Blanchette, K. Al-Haddad, A Generic Electrothermal Li-ion Battery Model for Rapid Evaluation of Cell Temperature Temporal Evolution, IEEE Trans. Ind. Electron. 64 (2) (2017) 998–1008.
[46] S.N. Motapon, E. Lachance, L.-A. Dessaint, K. Al-Haddad, A generic cycle life model for lithium-ion batteries based on fatigue theory and equivalent cycle counting, IEEE Open J. Ind. Electron. Soc. 1 (2020) 207–217.
[47] M. Pirani, P. Thakkar, P. Jivrani, M.H. Bohara, D. Garg, A Comparative Analysis of ARIMA, GRU, LSTM and BiLSTM on Financial Time Series Forecasting, in: 2022 IEEE International Conference on Distributed Computing and Electrical Circuits and Electronics, ICDCECE, 2022, pp. 1–6.
[48] J.L. Elman, Finding structure in time, Cogn. Sci. 14 (2) (1990) 179–211.
[49] S. Hochreiter, J. Schmidhuber, Long short-term memory, Neural Comput. 9 (8) (1997) 1735–1780.
[50] M. Schuster, K.K. Paliwal, Bidirectional recurrent neural networks, IEEE Trans. Signal Process. 45 (11) (1997) 2673–2681.
[51] Z. Sherkatghanad, A. Ghazanfari, V. Makarenkov, A self-attention-based CNN-Bi-LSTM model for accurate state-of-charge estimation of lithium-ion batteries, J. Energy Storage 88 (2024) 111524.
[52] Y. Ma, Z. Huang, J. Su, H. Shi, D. Wang, S. Jia, W. Li, A multi-channel feature fusion CNN-Bi-LSTM epilepsy EEG classification and prediction model based on attention mechanism, IEEE Access 11 (2023) 62855–62864.

Jarin Tasnim received her B.Sc. (2022) degree in Electrical and Electronic Engineering from Bangladesh University of Engineering and Technology (BUET). She currently works as a research assistant for the project ‘Development of smart fast chargers and virtual testing platform for electric vehicle batteries’ in Research and Innovation Centre for Science and Technology (RISE), BUET. Her research focuses on Signal Processing, deep learning, machine learning in smart healthcare, data analysis, and image processing.

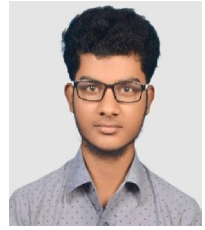

Md. Azizur Rahmanis a senior year student of the Electrical and Electronic Engineering Department, Bangladesh University of Engineering and Technology (BUET). His research interests include machine learning, deep learning, state of health and state of charge of electric vehicle batteries.

Md. Shoaib Akhter Rafi received his B.Sc. (2024) degree in Electrical and Electronic Engineering from Bangladesh University of Engineering and Technology (BUET). He currently works as a research assistant for the project ‘Development of smart fast chargers and virtual testing platform for electric vehicle batteries’ in Research and Innovation Centre for Science and Technology (RISE), BUET. His research focuses on Signal Processing, deep learning, machine learning in smart healthcare, data analysis, and image processing.

Muhammad Anisuzzaman Talukder joined EEE, BUET as a lecturer in early 2001, and has been serving as a Professor since 2014. He is also the director of Research and Innovation Centre for Science and Technology (RISE), BUET. He holds a Visiting Professor position at the University of Maryland, USA. During 2016-2018, he was with the University of Leeds, UK as a distinguished Marie-Curie Individual Fellow. He was an Honorary Fellow in the Hong Kong Polytechnic University during 2013-2015 and a Visiting Academic Fellow in the City University London, UK in 2013. He is a senior member of IEEE and a member of OSA, APS, and IEB. He has published more than 100 articles in highly reputed journals and conferences and has given several invited talks. He has earned significant research funds in Bangladesh, USA, and European Union. His research interests include, nanophotonics, biosensors, photovoltaics, plasmonic lasers, quantum cascade lasers, applications of mid-infrared technologies for health and environment, solar hydrogen generation, digitalization of battery testing, and energy modeling.

Md. Kamrul Hasan received the B.Sc. and M.Sc. degrees in electrical and electronic engineering from Bangladesh University of Engineering and Technology (BUET), Dhaka, Bangladesh, in 1989 and 1991, respectively, and the M.Eng. and Ph.D. degrees in information and computer sciences from Chiba University, Chiba, Japan, in 1995 and 1997, respectively. In 1989, he joined the Department of Electrical and Electronic Engineering, BUET, as a lecturer, where he is currently a professor. He was a Post-Doctoral Fellow and a Research Associate with Chiba University, and Imperial College London, London, U.K., respectively. He was a short-term Invited Research Fellow with the University of Tokyo, Tokyo, Japan, and a Professor of International Scholars with Kyung Hee University, Seoul, South Korea. He is a Senior Member of IEEE and Fellow, Bangladesh Academy of Sciences. He has authored or coauthored over 130 scientific publications. His current research interests include digital signal processing, adaptive filtering, speech and image processing, medical imaging, quantitative tissue characterization, artificial intelligence in healthcare, and battery management systems. Dr. Hasan is currently an Associate Editor of IEEE ACCESS.